2008

Development of thin CsHSO4 membrane electrode assemblies for electrolysis and fuel cell applications

Lars E. Ecklund-Mitchell

University of South Florida

Scholar Commons Citation

Ecklund-Mitchell, Lars E., "Development of thin CsHSO4 membrane electrode assemblies for electrolysis and fuel cell applications" (2008). *Graduate Theses and Dissertations.*
http://scholarcommons.usf.edu/etd/225

Development of Thin $CsHSO_4$ Membrane Electrode Assemblies for Electrolysis and Fuel Cell Applications

by

Lars E. Ecklund-Mitchell

A thesis submitted in partial fulfillment
of the requirements for the degree of
Master of Science in Chemical Engineering
Department of Chemical Engineering
College of Engineering
University of South Florida

Major Professor: John T. Wolan, Ph.D.
Burton Krakow, Ph.D.
Elias K. Stefanakos, Ph.D.
Aydin Sunol, Ph.D.

Defense Date:
October 3, 2008

Keywords: solid acid, electrolyte, methanol, hydrogen, MEA

Acknowledgments

No one makes a journey entirely unassisted. I owe any success that I meet from this work from the many people who gave me support, encouragement, and advice. First of all, my parents, without whom I could not have even begun on this great adventure. I would also like to thank Drs. Wolan and Krakow, whose advice and support provided motivation and direction for this project. Finally, all my colleagues in the Applied Surface Science Lab and Fuel Cell Research Lab, but specifically Benjamin Grayson, Eric Weaver, Don Payne, Timothy Fawcett, Ala’a Kababji, and Jonathan Mbah for their friendship and for providing technical assistance, editing, and sounding boards for my ideas.

Thank you to all.

Table of Contents

List of Tables

List of Figures

Development of Thin $CsHSO_4$ Membrane Electrode Assemblies for Electrolysis and Fuel Cell Applications

Lars E. Ecklund-Mitchell

ABSTRACT

In this work the use of the solid acid $CsHSO_4$ as an electrolyte in a hydrogen/oxygen fuel cell or the disassociation of water into hydrogen and oxygen has been investigated. Several issues have been cited in literature regarding the use of $CsHSO_4$ as a solid electrolyte; these include: difficulty interpreting proton conductivity profiles of real membranes, high permeability of the membrane to fuel and product gases, and low mechanical strength. In an attempt to improve our understanding and possibly eliminate these issues, performance characteristics of prepared $CsHSO_4$ membranes have been investigated utilizing various methods of synthesis and membrane fabrication. A consistent method of $CsHSO_4$ membrane construction was developed based on these investigations. In addition, a novel method of sintering to decrease the membrane’s permeability to fuel gases was developed and evaluated. The effects of these measures were investigated and tested in a prototype cell for proof of concept of fuel cell and electrolysis applications.

1 Introduction

The main objective of this work is the investigation of the viability of solid acid electrolytes, specifically cesium hydrogen sulfate, for use in thin membrane electrode assemblies (MEAs) for improved performance in fuel cell or electrolysis applications. The formal introduction will describe solid acid electrolytes and how their structure, bonding types, and internal order-disorder determine their proton conductivity character. Moving from these general considerations, the structure and properties of cesium hydrogen sulfate in particular will be addressed, showing the reasoning behind its selection as the electrolyte to be studied. Considerations for the use of cesium hydrogen sulfate in membrane electrode assemblies, and finally discussion of overall design considerations for electrolysis and fuel cell applications will be addressed.

The overall structure of this work will then present the three major project areas explored. Firstly, the analysis of different synthesis methods for cesium hydrogen sulfate with the verification and characterization of the resulting materials by a variety of solid state methods will be presented. Second, the effect of pressing and sintering methods on the gas permeability of cesium hydrogen sulfate will be shown and discussed. Finally, the knowledge gained from the above noted investigations will be used to fabricate, characterize, and test prototype membrane electrode assemblies for performance metrics. A detailed discussion of results, conclusions and suggestions for future work will be given.

1.1 Solid Acid Electrolytes and $CsHSO_4$

An electrolyte is a medium in which charge transfer is produced by the mobility of ions, charged particles, through that medium. Electrolytes, which may exist as solutions, gases, molten liquids, or solids, do not allow direct electrical conduction. When an electrical potential is applied to the electrolyte a chemical reaction near the sources of the potential strips or adds electrons to mobile species within the electrolyte. These charged species may then travel through the electrolyte to neutralize charge build up near the electrodes.

Solid electrolytes are electrolytes that allow the transfer of charged ions through their solid structure. Often these materials are polymers or ceramics. Larger ion species are typically constrained within the solid structure by direct bonding, as well as small pore size. Conduction of charge is therefore accomplished by the transfer of smaller ionic species, often single protons. Solid acids have advantages of being self-supporting, not requiring the greater support as molten or liquid electrolytes. Also unlike molten or liquid electrolytes, solid electrolytes are not subject to mass transfer of the electrolyte medium to reactant or product gases by evaporation. Finally, with proper process design, a solid electrolyte can form a barrier between reactant and product gases, either creating a pure product gas or a mixture that can be easily separated. This can drastically reduce costs associated with separation and purification of process gases[1].

A solid acid electrolyte ideally displays the high ionic conductivity of an acid with the advantage of a solid matrix at standard operating temperatures and pressures.

Cesium hydrogen sulfate ($CsHSO_4$) has been investigated as a solid acid electrolyte by several authors recently[2-6]. $CsHSO_4$ belongs to a category of solid acid electrolytes known as $MHXO_4$ type solid acids. The M represents an atom in the alkali group, such as potassium or rubidium, while the X is atom of the chalcogen group such as sulfur or selenium. Thus, in addition to $CsHSO_4$, potassium hydrogen selenate ($KHSeO_4$) and sodium hydrogen sulfate ($NaHSO_4$) are representatives of this classification. These solid acids are characterized by structures composed of alternating cations and oxy-anions, where the ratio of the two is 1:1, with the oxy-anions bounded by hydrogen bonding throughout the structure. The ratio of hydrogen atoms to oxy-anions within the structure (1:1), directly impacts the electrical character of these materials depending on the number of nearest neighbor oxy-anions around a given oxy-anion, as shown in the subsections below.

Previous work with $CsHSO_4$ includes study of proton conductivity in the superprotonic phase[3, 5-9], study of the phase transitions and phase diagrams of $CsHSO_4$[10-16], modeling of the molecular structure of room-temperature and superprotonic $CsHSO_4$[17-19], developments in the high-temperature stability of $CsHSO_4$ under a variety of atmospheres[20], and the construction of H_2/O_2 fuel cells[2, 4]. The result is a body of knowledge that describes the electrical properties, phase transition temperatures and energies, and expected structural measurements of $CsHSO_4$.

The construction of a working H_2/O_2 fuel cell using $CsHSO_4$ has been successfully reported[2, 4]. In addition, certain difficulties, including the formation of consistent membranes, adhesion of electrodes and catalyst layers, cross-barrier diffusion of fuel gases, the relative fragility of manufactures membranes, and the stability of membranes under different atmospheres at high temperature, involving the use of $CsHSO_4$ have hampered attempts, requiring novel solutions to preparation and operating conditions.

1.1.1 Structure

The structure of solid acids can be described using the principles of atomic bonding, coordination, and order-disorder. These three factors describe how the structure of solid acids arises, and also how the properties of solid acids, particularly their changes in phase and resulting changes on electrolytic behavior, arise.

Solid acids adhere to the general chemical formula: $M_aH_b(XO_4)_c$, where M is a monovalent or divalent cation, XO_4^{-2} is a tetrahedral oxy-anion, and a, b, and c are integers. Structurally, solid acids are typically described as two overlapping lattices, the hydrogen-bonded tetrahedral oxy-anions (XO_4^{-2}) making up one lattice, interspersed with a second lattice of the cations (M^+) resulting in a charge balance.

At low temperatures, $CsHSO_4$ has a monoclinic structure of stacked chains of SO_4^{-2} and Cs^+ ions. Two such phases have been observed[18, 19], both monoclinic but with different unit cell parameters. These phases are labeled $CsHSO_4$-III for the lower temperature phase, and $CsHSO_4$-II for the higher temperature phase. The transition temperature for these two phases ranges from 69 to 73 °C. A monoclinic structure of $CsHSO_4$ is shown in Figure 1.1.

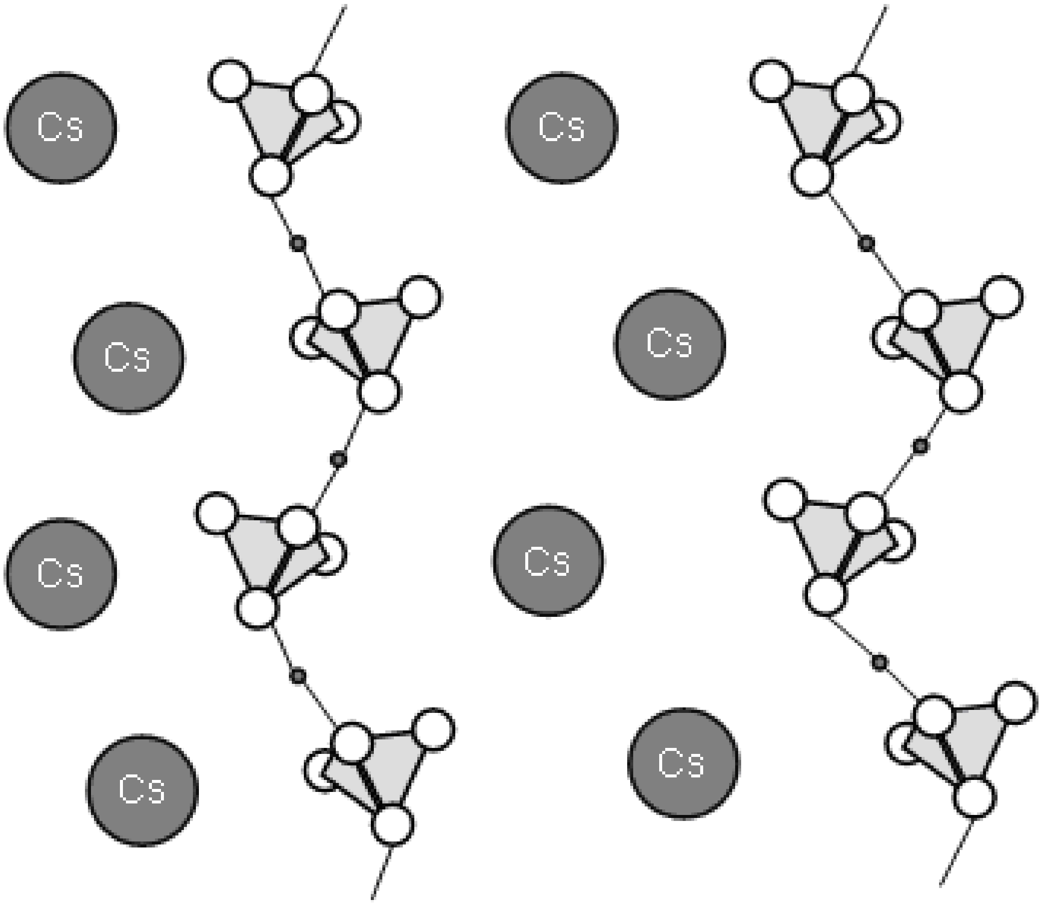

Figure 1.1 Structure of $CsHSO_4$ at Room Temperature Phase
The monoclinic structure of $CsHSO_4$-III or $CsHSO_4$-II, present from room temperature to 140-145º C.

At higher temperatures (in excess of 145 °C) $CsHSO_4$ exists as a solid phase tetrahedral structure. The Cs^+ and SO_4^{-2} ions form two interlocking three dimensional tetrahedral matrices with neutral charge distribution. This phase is labeled $CsHSO_4$-I. A tetrahedral $CsHSO_4$ structure is shown laterally to illustrate nearest neighbors of the SO_4^{-2} matrix in Figure 1.2.

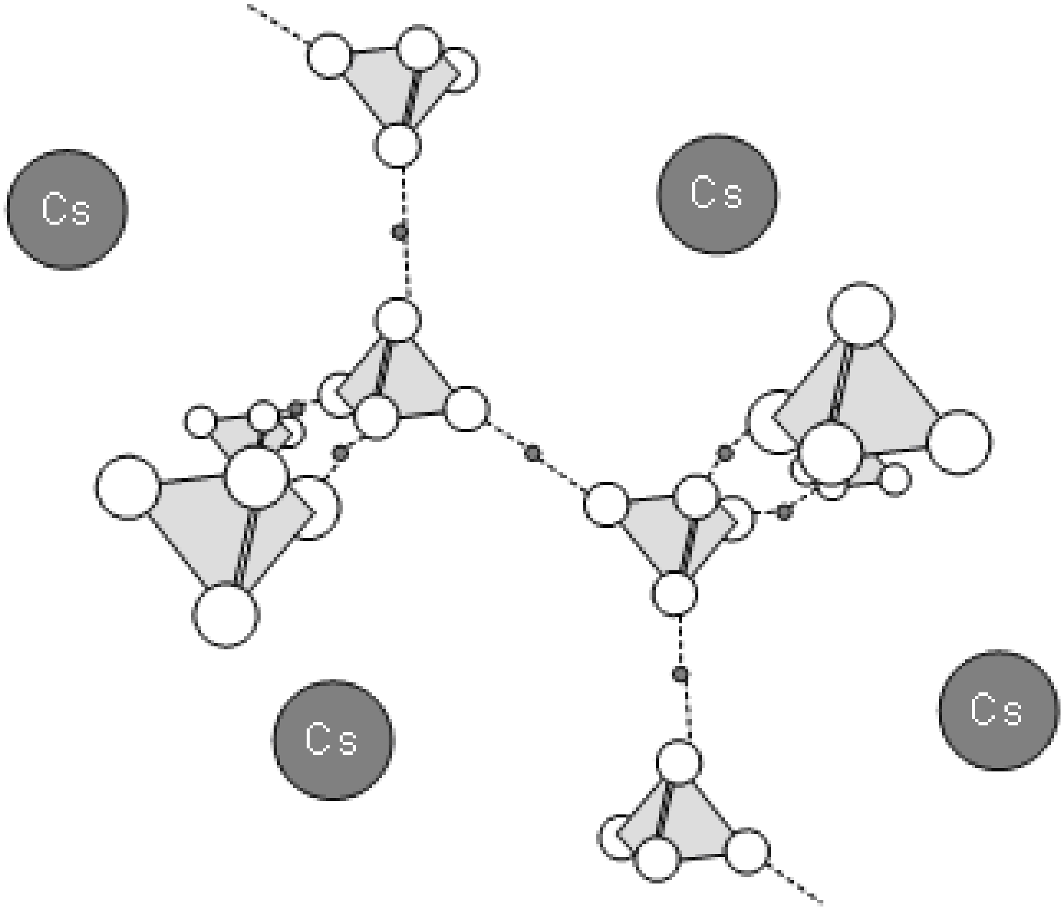

Figure 1.2 Structure of $CsHSO_4$ at High Temperature Phase
The tetrahedral structure of $CsHSO_4$-I, present at temperatures above 145° C.

1.1.1.1 Bonding[21]

The structure of solids is dominated by the interactions resulting from atomic bonding between constituent atoms in the solid. These bonds are a consequence of electronic forces between negatively charged outer shell electrons and the positively charged nuclei of the atoms. These bonds are classified into categories of electrostatic bonding, between positively and negatively charged ions due to electron transfer, covalent bonding, a result of electron sharing between two atoms, and metallic bonding, attraction due to delocalized electrons. These categories do not describe all possible bonding as observed bonding may exhibit character of more than one type.

Of these types of bonds, the electrostatic bond, also known as ionic bonding, best describes the bonding in $CsHSO_4$, like solid acids in general. Electrons are transferred locally from electropositive cesium to the electronegative species, SO_4^{-2}, creating a charge imbalance resulting in an electrostatic force. This creates a strong overall pattern of alternating anion and cation within the structure of the solid, a three-dimensional pattern dictated by the electrostatic attraction between positively and negatively charged elements resisting the repulsion of like-charged elements to set the size and distance between elements within the overall matrix.

The other important type of bonding in solid acids is hydrogen bonding. In hydrogen bonding, the attraction of an atom of hydrogen to two atoms acts as a bond between them. The hydrogen atom acts as a sort of “bridge.” This type of bonding is much weaker than ionic bonding, but still has a large effect on the shape and properties of the solid. Hydrogen bonding can be described by its intra-hydrogen bonding, the local geometries of the hydrogen about the two atoms being bonded, and the inter-hydrogen bonding, the overall spatial geometry of the solid lattice[22].

In $CsHSO_4$, hydrogen bonding occurs between two oxygen atoms on adjacent SO_4^{-2} groups. The intra-hydrogen bond geometry between the two oxygen atoms participating in the bonding, and the hydrogen atom, vary in strength with distance and the covalency of the bonding. At closer distances, the hydrogen bond is stronger, with a more covalent character. The single valance electron of the hydrogen is shared between the two oxygen atoms. As the inter-oxygen atom distance increases, the bond strength decreases and the hydrogen atom becomes more firmly attached to one of the oxygen atoms, creating a charge imbalance across the bond, resulting in a more ionic character. At certain bond lengths, the hydrogen atom can switch positions between two energy wells along the bond, creating hydrogen bond disorder. This is only seen at a discrete range of bond lengths—at longer bond lengths the hydrogen closely attaches to one of the oxygen atoms, and the energy required to jump to the other potential well is greater than the actual bond strength, while at shorter bond lengths the hydrogen atom is equally shared between the two bonding oxygen atoms. These bonds strengths and corresponding characters are summarized in Table 1-1.

Table 1-1 Correlation Between Hydrogen Bond Types and Bond Character[22]

Bond Strength	Interoxygen distance (Å)	Character	Hydrogen Bond Disorder
Strong	≤ 2.4	covalent	Not observed—hydrogen is shared
Medium	2.4 – 2.9	polar covalent	Can be observed at higher temperatures
Weak	≥ 2.9	ionic	Not observed—bond is too weak

Because the ratio of hydrogen bonds to SO_4^{-2} groups is one to one, traditional predictions would describe the structure of $CsHSO_4$ as cyclic dimmers, rings, or chains. This is because of the generally accepted rule relating the ratio of hydrogen to tetrahedral oxy-anions. In this regime, the dimensionality of the network is related to the density of hydrogen bonds by:

$$D = 2 \times \left(\frac{H^{+}}{XO_4^{-2}} \right) - 1$$

Where D is the dimensionality of the lattice, (H^+/XO_4^{-2}) is the ratio of hydrogen atoms (or hydrogen bonds) to oxy-anion tetrahedrals, in this case SO_4^{-2} groups. As we will see, this accurately describes $CsHSO_4$ in the lower temperature phase, but other factors lead to a different structure in the higher temperature phase.

1.1.1.2 Order-Disorder[21]

The discussion of order-disorder concerns the effects on the structure and properties of a solid when a species partially occupies more than one position within the solid structure. The given species will be energetically stable in more than one position, and will oscillate between the two positions. A hierarchal system exists for the classification of disorder within a solid lattice, with the two main types being structural disorder, which looks at the multiple positions that can be occupied by a single species, and chemical disorder, involving a single position but multiple species. Structural disorder is further classified as static disorder, in which the basic structure of the solid includes multiple positions that a given species may occupy, with a randomized distribution based on local factors, and dynamic disorder, in which the disorder of the species arises as it is energetically excited into a state in which freely can move between multiple positions.

The superprotonic conduction ability of $CsHSO_4$ at higher temperatures is due to the dynamic disorder created as the lattice is thermally excited. The disorder created is expressed throughout the crystal lattice, and is described using two classifications based on the two species that are involved.

Inter-hydrogen bond disorder is disorder created as the structure of $CsHSO_4$ changes upon heating. Multiple positions for hydrogen bonding between SO_4^{-2} anions become available as the crystal lattice changes from a monoclinic structure at low temperature to a tetrahedral structure at high temperature. This phase transition increases the number of nearest neighbor SO_4^{-2} anions around any given SO_4^{-2} anion from two to four, and the ratio of possible inter-hydrogen bonds to SO_4^{-2} anions from one to two. This allows for the transition of hydrogen bonds between the available crystallographic positions, dramatically changing the proton conduction character of the solid.

Strongly related to the change in inter-hydrogen bond disorder is an increase in oxy-anion disorder. The orientation of the SO_4^{-2} anion within its location in the crystal lattice is subject to constraints based on hydrogen bonding and van der Waals forces from neighboring ions. After the transition to the higher temperature tetrahedral phase, the constraints of hydrogen bonding are relaxed due to the increase in inter-hydrogen bond disorder. At the same time, van der Waals forces from neighboring SO_4^{-2} anions and cesium cations is normalized from a linear mode in the monoclinic, to a more diffuse three-dimensional mode in the tetrahedral. Certain orientations of the SO_4^{-2} anion are still preferred, but the energy barriers that separate them are much lower, allowing easy, thermally excited transitions between them. As a result, the SO_4^{-2} anion may freely rotate about its location in the crystal lattice after $CsHSO_4$ takes a tetrahedral structure.

1.1.2 Proton Conductivity

Proton conduction through solid acids is several orders of magnitude higher than that of electron conduction. This allows solid acids to be used in applications as proton transport membranes while also acting as electrical insulators. This feature is a defining behavior for a successful electrolyte in a membrane electrode assembly.

Table 1-2 shows typical values for solid acid electrical and proton conductivities.

Table 1-2 Comparison of Electronic and Ionic Conductivity[23]

Electronic Conductivity	Ionic Conductivity
Conductivity range 10 S/cm $< \sigma < 10^{5}$ S/cm	Conductivity range 10^{-3} S/cm $< \sigma <$ 10 S/cm
Electrons carry current	Ions carry current
Conductivity increases as temperature decreases	Conductivity decreases as temperature decreases

Solid acids display five general methods for proton transfer: atomic diffusion, proton-displacement, molecular reorientation, vehicle mechanism, and the Grotthus mechanism[4]. The mechanism which dominates in that solid acid is determined by the acid's structure, electron density, the diffusivity of larger atomic species through the solid lattice, and the rotational frequency of cation groups.

Atomic diffusion is only possible in those materials where the proton can share electron density with the host material. The proton then diffuses through the lattice coupled with the diffusion of electrons. These materials have high electron mobility, and are therefore electrically conductive. Thus they make poor electrolytes.

Proton displacement is triggered when protons become thermally excited to energy levels above the height of the surrounding potential well they typically occupy within the lattice. This creates ferroelectric behavior in solid acids as electric forces change faster then elastic forces can compensate, creating a shift in ion position and a dipole moment within the structure. This effect shows hysterisis behavior when the applied heat is removed. Only a few solid acids show this behavior, and it is generally at too low of a level for an electrolyte application.

Molecular reorientation, the vehicle mechanism, and the Grotthus mechanism all involve the proton attaching to a larger molecular or ionic species. The motion of this larger species within the solid lattice provides the primary motive transport for the proton. These mechanisms have the advantages of being independent of the electrical conductivity of the material while still allowing for fast proton transport.

In molecular reorientation the proton is transported by a molecular species undergoing a rotation within the solid lattice. This allows the proton to “jump” between multiple locations within the crystal structure. The rate of proton transfer is then limited by the ability of protons to attach to whole molecular species, as well as the dynamics of the molecular species.

The vehicle mechanism involves the proton bonding with a molecular or ionic species with the capability to diffuse throughout the solid. These larger species act as carriers, while their diffusivity within the lattice determines the rate of proton transfer. To maintain equilibrium within the solid, empty carriers must move counter to the direction of proton transfer, forming a kind of "conveyor belt" of molecular or ionic species carrying the protons through the solid.

The Grotthus mechanism combines features of proton displacement and molecular reorientation. Unlike molecular reorientation, the proton bonds with an oxy-anion whose rotation within the matrix transports the proton between two crystalligraphically equivalent positions. From here the proton undergoes a displacement along the hydrogen bond with the former oxy-anion to a closer position to a second oxy-anion. This second oxy-anion then undergoes a similar rotation and the proton moves to another position within the crystal. In this way the proton "hops" from rotating oxy-anion to oxy-anion. This requires that the oxy-anions possess a high degree of dynamic mobility within the lattice, but it has been determined that the proton displacement between oxy-anion occurs at a frequency three orders of magnitude less then the rotational rearrangement of oxy-anions, making it the rate limiting step.

The Grotthus mechanism is illustrated in Figure 1.3 below.

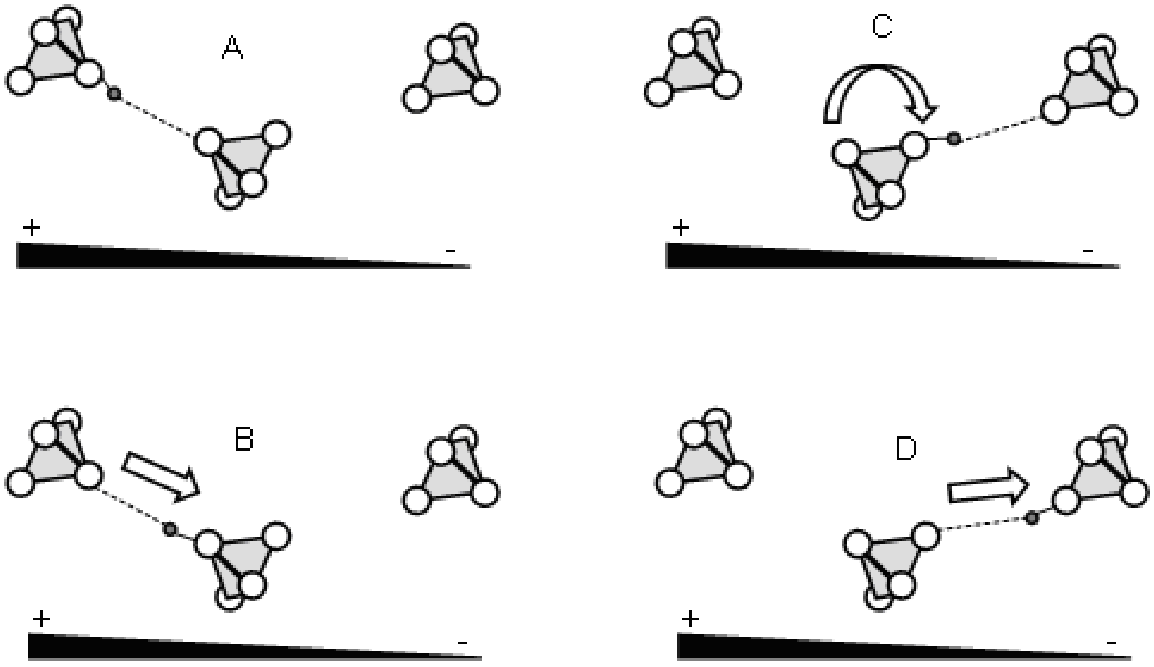

Figure 1.3 The Mechanics of Proton Conduction in $CsHSO_4$
The Grotthus mechanism of proton conduction in $CsHSO_4$. A proton transfers along hydrogen bonding between two adjacent SO_4^{-2} groups (B). The SO_4^{-2} group rotates bringing the attached proton into proximity with a different SO_4^{-2} group (C). The proton then transfers along the newly formed hydrogen bond to the next SO_4^{-2} group (D).

1.1.3 Phase Transitions

Because $CsHSO_4$ undergoes such a remarkable change in proton conductivity when transitioning from the lower temperature to the higher temperature phase, the mechanics of this phase change are of interest and will be briefly discussed here.

The phase transition of $CsHSO_4$ from monoclinic $CsHSO_4$-II to tetrahedral $CsHSO_4$-I is a first order solid-solid transition. Since this is a first order change, the changes in extensive thermodynamic variables are negligible compared to the discontinuous change in entropy. This allows the use of Differential Scanning Calorimetry (DSC) to characterize the thermodynamics of the transition.

Although this transition is a solid-solid transition, the change in physical properties between the two phases is similar to that of a solid-liquid transition. Specifically, the increased order-disorder in the tetrahedral SO_4^{-2} ions leads to a malleable superprotonic phase, variously described as being similar to “clay or plasticine.” The room temperature phase, on the other hand, is a solid crystalline structure, brittle and prone to fracture in the aggregate.

Figure 1.4 below, shows the typical proton conductivity behavior of $CsHSO_4$ with increasing temperature and phase change.

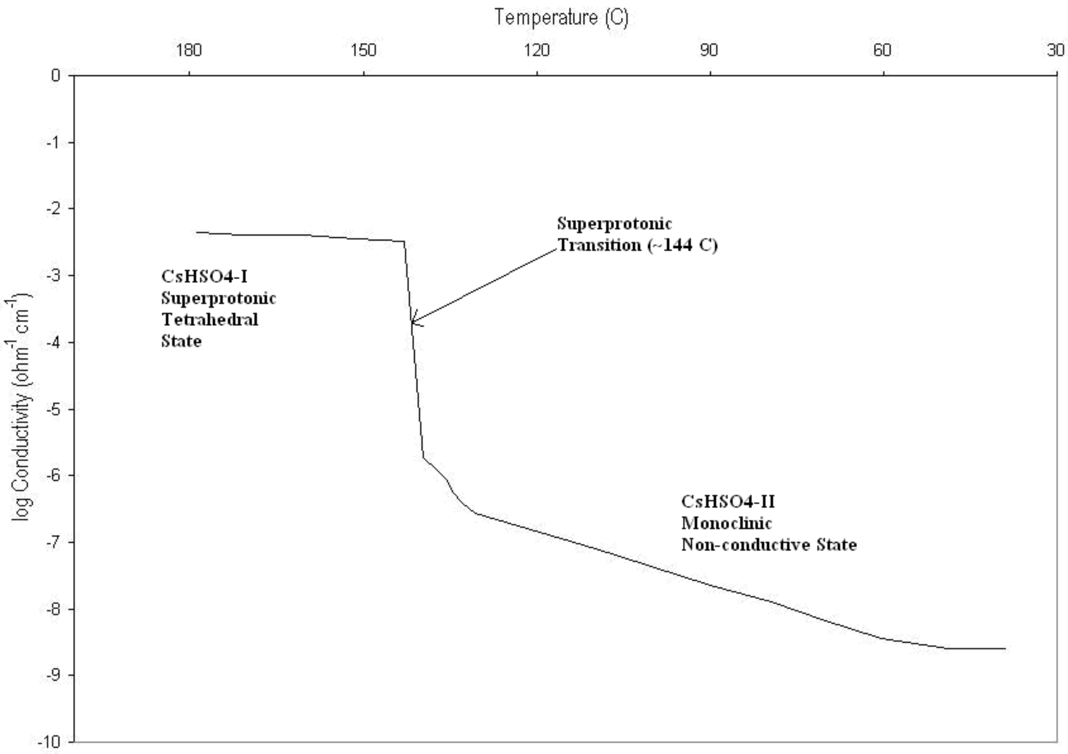

Figure 1.4 $CsHSO_4$ Proton Conductivity from Boysen[4]
Typical proton conductivity behavior of $CsHSO_4$. Note linear (near-linear on this plot) behavior within a given phase, contrasted with the sharp rise in proton conductivity associated with the superprotonic transition.

1.2 Applications

Solid acid electrolytes have been investigated for their use in traditional electrolyte applications, namely, as fuel cell electrolytes and for active electrolysis. These two possible applications for solid acids are discussed in more detail below, considering currently used electrolyte materials.

1.2.1 Fuel Cells

Fuel cells are devices that convert a chemical change into an electric current by harnessing the transfer of ionic motion and the resulting electric potential. Fuel streams react to produce ions, which must move through an electrolyte to complete the chemical reaction. This motion through the electrolyte creates a charge imbalance between the two sides of the electrolyte barrier, which creates an electric current. In this way, a fuel cell resembles an intermediary device between a battery, which produces electric potential due to internal chemical reaction, and a combustion engine, which uses the energy released by the chemical reaction of fuel streams[24].

Many types of fuel cells have been put to use in a variety of applications. Solid acids in general, and $CsHSO_4$ in particular, are used in a type known as proton exchange membrane (PEM) fuel cells. The acronym PEM is occasionally interpreted as "Polymer Electrolyte Membrane" given the widespread use of commercial polymer electrolytes such as Nafion© in commercial fuel cells. Fuel cells of this type are also often grouped as part of Ion Exchange Membrane (IEM) fuel cells, although that group also includes those whose electrolyte barriers can transfer larger ion complexes than just protons.

A vital component in a fuel cell is the electrolyte barrier that separates the initial reactants. In a fuel setup, the electrolyte forms part of a combined electrode/catalyst/electrolyte complex commonly called a membrane electrode assembly (MEA). The construction of MEAs results in a complex interdependent series of considerations including the chemical compatibility and kinetics of fuel streams, electrode materials, catalyst materials and deposition techniques, and the electrolyte itself[25, 26].

The internal mechanism of a PEM fuel cell is best described by using an example. Consider a cell for the reaction of hydrogen and oxygen to produce water. The overall reaction for this fuel cell is:

$$2H_2 + O_2 \rightarrow 2H_2O$$

The reaction at the anode is the dissociation of hydrogen to adsorbed hydrogen atoms and electrons.

$$2H_2 \rightarrow 4H^+ + 4e^-$$

The electrons follow an external path to the cathode, creating an electric current through a load. The hydrogen atoms migrate through the membrane to the cathode, where they recombine with the electrons and adsorbed oxygen to produce water.

$$4H^+ + 4e^- + O_2 \rightarrow 2H_2O$$

A schematic of a hydrogen-oxygen fuel cell is shown in Figure 1.5.

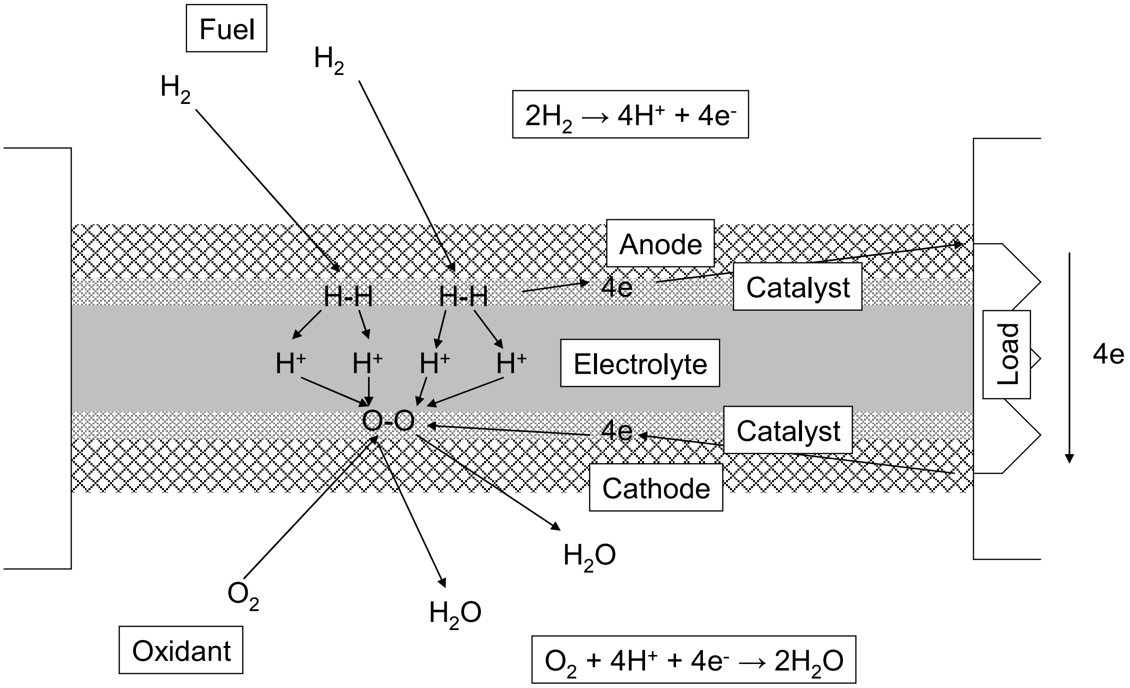

Figure 1.5 Diagram of a Hydrogen Fuel Cell
Hydrogen fuel enters and reacts in the anode chamber, resulting in H^+ ions that migrate through the electrolyte, where they react with oxygen in the cathode chamber to produce water. A current of electrons is produced through a load connecting the two electrodes.

The total Gibbs free energy of the reaction in the cell is the sum of these two half reactions:

$$2H_2 \rightarrow 4H^+ + 4e^- \qquad \Delta G_f^\circ = 0.0\frac{kJ}{mol}$$

$$4H^+ + 4e^- + O_2 \rightarrow 2H_2O \qquad \Delta G_f^\circ = -482.6\frac{kJ}{mol}$$

$$2H_2 + O_2 \rightarrow 2H_2O \qquad \Delta G_{rxn}^\circ = -482.6\frac{kJ}{mol}$$

The total Gibbs free energy of the fuel cell reaction is related to the theoretical open cell voltage by the Nernst equation:

$$\Delta G^{\circ}_{rxn} = -nF\varepsilon^{\circ}_{0}$$

where ΔG^{o}_{rxn} is the change in standard Gibbs free energy for the reaction, n is the number of charge carriers, F is Faraday's constant, and ε^{o}_{0} is the theoretical open cell voltage.

Open cell voltage at operating conditions, however, will be dictated by the temperature of reaction and the chemical activities of the reactants and products. The Nernst equation is expanded, to show these terms, thus:

$$\varepsilon_{rev} = \varepsilon^{\circ}_{0} + \frac{2.303RT}{nF}\log_{10}\frac{[R]^{s}}{[P]^{q}}$$

Where ε_{rev} is the theoretical reversible cell potential at the operating conditions, T is the absolute temperature, [R] and [P] are the chemical activities of the reactant and product, respectively, and q and s are the coefficients of reaction for the reactant and product, respectively. The theoretical reversible cell potential accounts for the loss of electric potential due to the thermodynamic losses associated with reaction.

A maximum efficiency (E_{max}) of an electrochemical cell can then be defined as the ratio of the change in Gibb's free energy at the reaction temperature (ΔG_{T}), and the ideal change in enthalpy for the reaction (ΔH_{0}). Since the change in Gibb's free energy for an electrochemical cell nearly reduces to the electrical work, this efficiency can be conceptualized as the maximum amount of electrical work that can be produced out of the total chemical energy released in the reaction.

$$E_{\max} = \frac{\Delta G_T}{\Delta H_0}$$

An additional definition of efficiency is the voltage efficiency, the ratio of the observed voltage with the theoretical reversible cell potential. This efficiency shows losses that are not due to thermodynamic constraints because of operating conditions, but rather due to losses from the fuel cell and MEA design, or from polarization effects.

$$E_v = \frac{\varepsilon_{cell}}{\varepsilon_{rev}}$$

Finally, an overall efficiency can be defined as the product of the maximum and voltage efficiencies, showing the ratio of observed cell potential to the theoretical open cell voltage, combining losses due to thermodynamic and polarization effects.

$$E_{overall} = E_{\max} * E_v$$

Polarization effects in a fuel cell are dependent on several factors relating to the construction techniques of the fuel cell apparatus itself, the membrane electrode assembly, and the choice of electrolyte and operating conditions. The primary losses of power from a fuel cell are electrolyte conductivity, catalytic activity, gas transport to and from the surface of the electrolyte, and gas transport across the electrolyte barrier without reaction[27].

Loss of power due to electrolyte conductivity is termed *Ohmic polarization*, and is due to the resistance to proton transport of the electrolyte. At operating conditions, the electrolyte will behave as a proton resistor of a given resistance. At low currents, the amount of loss from Ohmic polarization is zero, but as current increases, measured voltage between electrodes decreases linearly, as transported protons through the electrolyte begin to equalize the electric potential. The slope of this relationship is equal to the measured resistance of an equivalent resistor from proton impedance measurements of the electrolyte. As proton conductivity of a given electrolyte is increased, the slope of this line decreases and higher measured potentials between the electrodes continue to persist at higher currents, resulting in higher power ($P = \varepsilon \times I$).

Loss of power due to catalytic activity is termed *activation polarization*, and is a result of the surface kinetics at the anode or cathode. A poor choice in catalyst, or a poisoned catalyst, at either electrode, can result in severe activation polarization. Loss of cell voltage decreases quickly with increasing current at low current values, as reduced reaction sites or poor electrolyte/catalyst compatibility increases the initial energy required for intermediate surface reactions. The losses due to activation polarization cause an initial drop in cell potential as current equilibriums within the immediate area of the electrodes are disrupted. As current increases, the relative change in current with voltage decreases, making these deviations from equilibrium less severe. However, initial loss of cell potential due to activation polarization can significantly reduce the overall potential of the cell as current is increased.

Gas transport to and from the electrode reaction areas can cause *concentration polarization* at higher currents. This can either be an issue of the fuel gas being consumed too quickly at the surface of the anode, setting up a concentration gradient between the bulk fuel gas in the anode compartment through the porous electrode, an issue of oxidant undergoing a similar concentration gradient in the cathode compartment due to the speed of reaction, or the product gas not diffusing quickly enough from the cathode surface to the bulk gas, setting up a concentration gradient in that direction. Concentration losses are primarily due to the latter situation, and are the result of slow gas diffusion of product away from the cathode. Since concentration polarization is due to quickly proceeding reactions, it is not seen until higher current.

Diffusion of fuel or oxidant gases across the electrolyte barrier can cause loss of cell potential or measured current. If the gases are diffusing without reaction, then less current will be observed simply because of lower conversion rates of fuel (imagining the fuel cell as a chemical reactor). If fuel or oxidant gases are penetrating a sufficient distance into the electrolyte and then undergoing reaction, this creates a larger zone of reaction with its local potential gradient than expected. This lowers measured cell potential at the electrodes, as the local potential gradient about the electrode actually extends into the electrolyte beyond the point at which it is observed by the electrode.

Figure 1.6 illustrates a typical current versus electric potential curve of a fuel cell (polarization curve), along with the effects of losses and peak power.

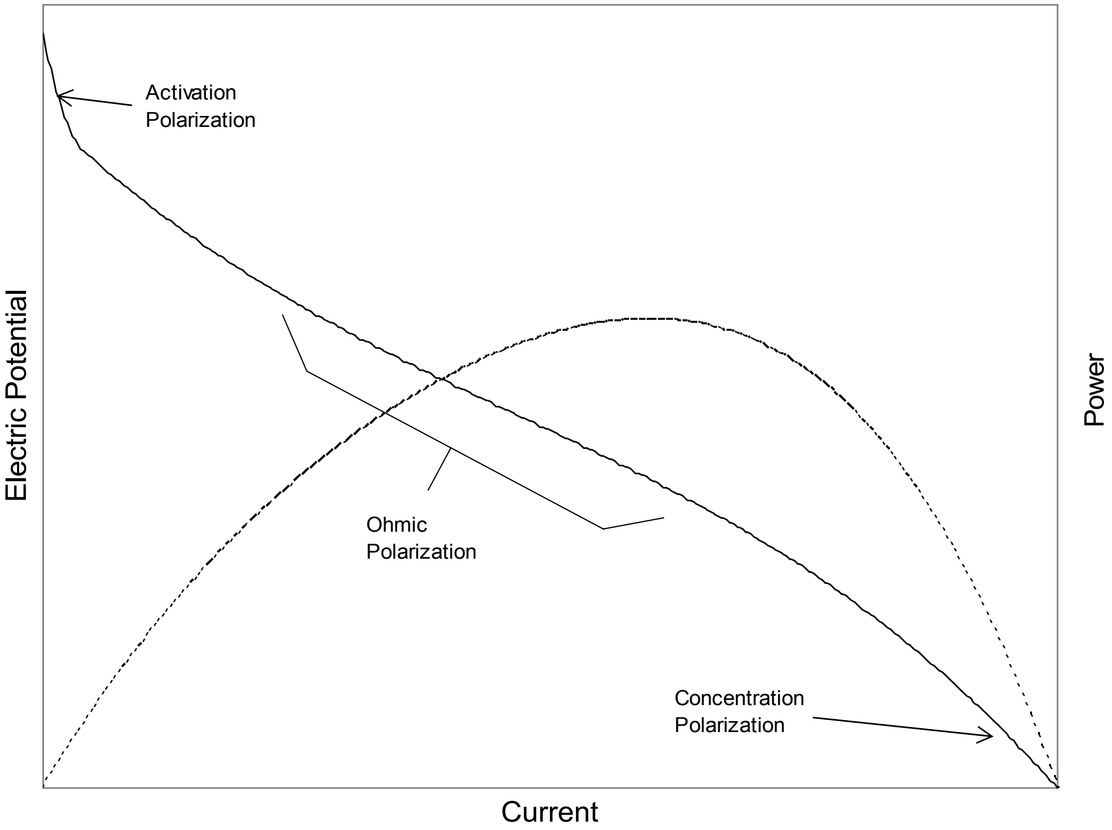

Figure 1.6 Polarization Losses in a Hydrogen Fuel Cell
A typical polarization curve for a fuel cell showing electric potential (solid line) and power (dotted line) versus current. Activation, Ohmic, and concentration polarization lowers the electric potential output by the cell with increasing current. All axis are in arbitrary units.

1.2.2 Electrolysis

Electrolysis, especially in the case of electrolysis performed with a solid electrolyte, can be thought of as a fuel cell operation in reverse. An electric current is used to create a chemical reaction. In a solid electrolyte setup, the reaction occurs at electrodes just as in a fuel cell, and results in ionic transport between the electrodes through the solid electrolyte. Thus, instead of inserting fuel and oxidant into the unit process and producing a current as output, a current is added to produce the reverse reaction.

Water can be electrolyzed as the opposite reaction to that in a H_2/O_2 fuel cell:

$$H_2O \rightarrow H_2 + \frac{1}{2}O_2$$

This reaction is usually carried out with water in the gas phase.

Many of the same considerations with regards to power loss in a fuel cell have an analogue to loss of efficiency in an electrolysis operation. As voltage between the electrodes increases, a minimum electric potential is reached at which the electrolysis process begins. In an ideal case, this voltage is equal to the ideal open cell voltage of a fuel cell operating with the reverse reaction. As the voltage increases, current passes through the circuit connecting the electrodes as ionic species move through the electrolyte, completing the reaction. As voltage is increased, activation losses due to ionic species in the electrolyte resisting the formation of further species at the electrode similar to that seen in a fuel cell are observed. For similar reasons as explained in the fuel cell section above, Ohmic losses due to the conductivity of the electrolyte to ionic species, and concentration losses due to mass transfer to and from the electrodes from the bulk of the inlet gases are also observed. These losses combine to shape the current versus voltage response of the electrolysis process. A maximum current is eventually reached at total conversion.

2 Development of a Solid Acid Electrolyte

The design and construction of the membrane electrode assembly is the primary objective of this work. To optimize the different steps in the construction process, a variety of techniques were employed. The individual steps taken and the methods employed to achieve those steps, are detailed in this section.

$CsHSO_4$ powders created by different variations of the synthesis methods were analyzed using thermal analysis (including differential scanning calorimetry, DSC, and thermo-gravimetric analysis, TGA), impedance spectroscopy, X-ray photoelectron spectroscopy (XPS), and powder X-ray diffraction (PXRD). Those results appear in the following subsections.

2.1 Synthesis of the Electrolyte

A standardized method for producing $CsHSO_4$ membranes was one of the primary goals of this work. To this end, various methods of chemically synthesizing $CsHSO_4$, crystallizing it out of solution, and pressing the resulting crystals into a membrane were explored.

2.1.1 Chemical Synthesis

Several methods of synthesis were employed for producing $CsHSO_4$. The first method reacted cesium sulfate, Cs_2SO_4, with sulfuric acid as shown below:

$$Cs_2SO_4 + H_2SO_4 \rightarrow 2CsHSO_4$$

An excess of sulfuric acid was used to insure the cesium sulfate progressed all the way to $CsHSO_4$.

A second method reacted cesium carbonate, Cs_2CO_3, with sulfuric acid by the following reaction:

$$Cs_2CO_3 + 2H_2SO_4 \rightarrow 2CsHSO_4 + H_2O + CO_2$$

Once again, an excess of sulfuric acid was used to insure complete reaction.

The second reaction was eventually abandoned in favor of the first. The evolution of CO_2 created splatters of heated sulfuric acid solution. In addition to this safety concern, as well as questions as to the extent of the reaction, lead to this decision.

2.1.2 Crystallization

$CsHSO_4$ was then crystallized out of solution using one of two methods. The first method used the slow evaporation of solution in an oven at 60 ºC to produce a highly concentrated solution. The solution container was then rapidly cooled to 10 ºC in a cold water bath, causing large crystals of $CsHSO_4$ to appear. The crystals were then quickly placed in a vacuum filter.

The second crystallization method took advantage of the insolubility of $CsHSO_4$ in most organic solvents. A large amount of methanol or acetone was added to the $CsHSO_4$ solution, typically resulting in 70-90 % methanol or acetone by volume. Small crystals of $CsHSO_4$ quickly formed as the concentration of methanol or acetone increased. These crystals were vacuum filtered, washing with methanol acetone. Crystals formed by acetone crystallization appeared quickly, as finely structured, fluffy crystals, floating at the interface between the water and acetone phases. When methanol was used, crystals formed in clumps at the bottom of the container, as the methanol dissolved into water creating a solution.

The second method of crystallization proved faster and easier to perform, and resulted in a greater percentage of the $CsHSO_4$ crystallizing out of solution. Also, the $CsHSO_4$ did not dissolve back into solution during the filtering process, which occurred in the first method as the samples warmed back up to room temperature. Finally, the crystals produced in the second method formed faster and were smaller then the crystals formed by the first method. This reduced entrapment of solution within the crystal structure, making drying easier. Later

DSC/TGA analysis of the crystals showed irregularities for the crystals that were grown with the first method. Those crystals formed with methanol instead of acetone were more difficult to dry completely, often requiring several cycles of drying in an oven and grinding with mortar and pestle before satisfactory material was obtained. For these reasons, the use of acetone to crystallize $CsHSO_4$ out of solution was adopted as standard practice in this work.

After crystals were produced, they were dried in an oven at 60 ºC for 10 to 12 hours. The powder was taken out and ground with a mortar and pestle at several points during the drying process. This was continued until the powder presented a uniform, dry appearance with minimal clumping and discoloration. The powder was then stored in a vacuum desiccator until use.

2.1.3 Pressing Methods

Powder was uniaxially compressed in a International Crystals Laboratory E-Z Press 12-ton hydraulic press, to achieve 50 MPa of pressure its surface as described by Boysen[4]. The pellet sizes were ½” in diameter, so the press was operated with 7.5 tons of force on the ram to obtain the desired pressure. The force was applied for ten to twenty minutes before the resulting pellet was removed. When 0.41 g of dry material was pressed, the resulting pellet had a density of 3.26 g/cm^3, and a thickness of 1 mm.

Since $CsHSO_4$ becomes a more malleable solid above the superprotonic transition temperature, these pressing conditions were duplicated on a Carver 4386 heated hydraulic press. It was discovered that the electrolyte stuck to stainless steel anvils after the heated pressing, making the removal of the pellet without damage extremely difficult. Using tungsten carbide anvils from International Crystal Laboratories with optically polished surfaces alleviated these problems.

Membranes produced with these methods were examined using optical microscopy. A typical micrograph of membranes pressed at room temperature and at heightened temperature is shown in Figure 2.1.

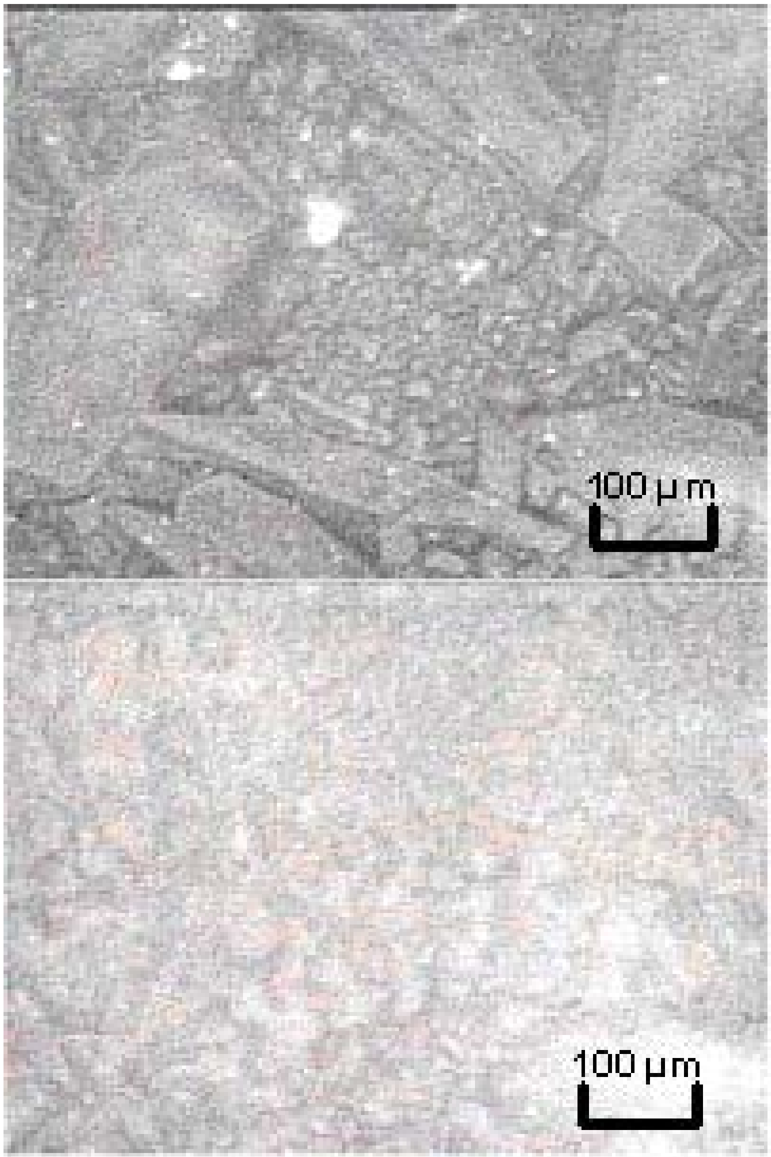

Figure 2.1 $CsHSO_4$ Membranes Pressed Under Ambient and Heightened Temperature x100
$CsHSO_4$ membranes pressed under ambient temperature conditions (top) versus those pressed under heightened temperature (bottom). Grain and flake size are larger, and better defined in the sample pressed at ambient temperature.

2.2 Impedance Spectroscopy

Impedance spectroscopy measures the proton conductivity of a sample against an intrinsic variable such as temperature. This gives a picture of the change in proton conductivity associated with a phase change in $CsHSO_4$.

This section will contain a discussion of the importance of impedance spectroscopy, and what we hope to accomplish by using it.

2.2.1 Proton Conductivity

Proton conductivity of the electrolyte is the primary indicator of the performance of the electrolyte in a fuel cell or electrolysis process. This is because the transfer of proton across the width of the electrolyte is the primary limiting step of the reaction.

The proton conductivity in solids can be described with the same models used for ionic conductivity. What follows is a brief description of ionic conductivity, and its dependence on temperature[28].

The conductivity (σ) of charge carriers in an isotropic solid can be described as the product of the concentration of charged carriers (n), the charge per carrier (q), and the charge carrier mobility (u) within the solid.

$$\sigma = nqu$$

A form of the Nernst-Einstein equation relates charge carrier mobility to the charge per carrier, the diffusion coefficient from Fick's first law describing the flux of particles through the solid (D) and the absolute temperature (T).

$$u = \frac{qD}{k_B T}$$

The diffusion coefficient can be described using a random walk model as the product of the frequency of charge carrier transfer (ω), the square of the distance between crystallographic sites (a_0) and a geometric factor depending on the structure of the solid (γ).

$$D = \gamma a_0^2 \omega$$

As the frequency of charge carrier transfer is a thermally activated process, it is best described as an Arrhenius-type temperature dependence.

$$\omega = \omega_0 \exp\left(\frac{-\Delta G_a}{k_B T}\right)$$

Where ν_0 is the attempt frequency of charge carrier transfer and ΔG_a is the Gibbs free energy for activation of charge carrier transfer.

Simplifying these equations we can arrive at an expression for the temperature dependence of conductivity within the solid:

$$\sigma T = A_0 \exp\left(\frac{-\Delta H_a}{k_B T}\right) = A_0 \exp\left(\frac{-\Delta E_a - P\Delta V_a}{k_B T}\right)$$

The pre-exponential factor, A_0, can be expressed in terms of constants associated with the charge carrier transfer.

$$A_0 = \frac{\gamma a_0^2 \omega_0 n q^2}{k_B} \exp\left(\frac{\Delta S_a}{k_B}\right)$$

with ΔS_a equal to the change in entropy for activation of charge carrier transfer. From these expressions, we can see that a plot of the log σT versus $1/T$ should produce a straight line, with the slope equal to the negative of the enthalpy for activation of the charge carrier transfer divided by the Boltzmann constant. This is valid as long as the crystal structure of the solid and its appropriate γ, a_0, and ν_0 values remain constant.

The conductivity of the sample is defined as the real admittance (reciprocal of the real resistance) divided by a geometric factor. In this case, the area of the sample exposed to the probe divided by the thickness of the membrane.

$$\sigma = \frac{1/R}{A/l}$$

It should be noted that with the conductivity of the material and cross sectional area of the pellet fixed, the real resistance is directly proportional to the thickness of the pellet.

2.2.2 Experimental Measurements

Impedance spectroscopy allows for the analysis of the real resistance and capacitance of a solid which might otherwise resist direct current measurements. The primary charge mobility in $CsHSO_4$ is carried by proton transfer, not electron mobility as in a typical conductor. Under direct current without a proton source, $CsHSO_4$ acts as an insulator, not yielding useful data. Impedance spectroscopy, however, allows the use of alternating current to determine the proton conductivity of the sample. Because there is no overall flow of electrons through the sample, the frequency and amplitude of the applied electric field become translated into the alternate movements of protons throughout the crystal lattice. This creates a measurable alternating current.

Typical impedance measurements employ a four probe technique applied to one surface of the sample. Either a linear or square configuration of probes is typically used, with a high current pass and a low current pass, allowing electrode potentials to be canceled out in the final data analysis.

Samples of $CsHSO_4$ were analyzed with impedance spectroscopy using an Agilent 4284A Precision LCR Meter in a two-point configuration. Half-inch diameter membranes of $CsHSO_4$ were manufactured, and then placed between two copper strip electrodes. An alternating electric potential at 1 MHz and one volt was imposed across the width of the membrane. The temperature of the sample was regulated using Linberg/BlueM MO1420SA-1 Mechanical Oven from 70 to 180 °C. Proton conductivity was calculated from the resulting resistance measurements.

Figure 2.2 shows proton conductivity versus temperature for three preparation methods used. Sample A is $CsHSO_4$ crystallized by acetone, sample B was crystallized by temperature variation, and sample C was crystallized by acetone, but pressed at heightened temperature, at 150 °C.

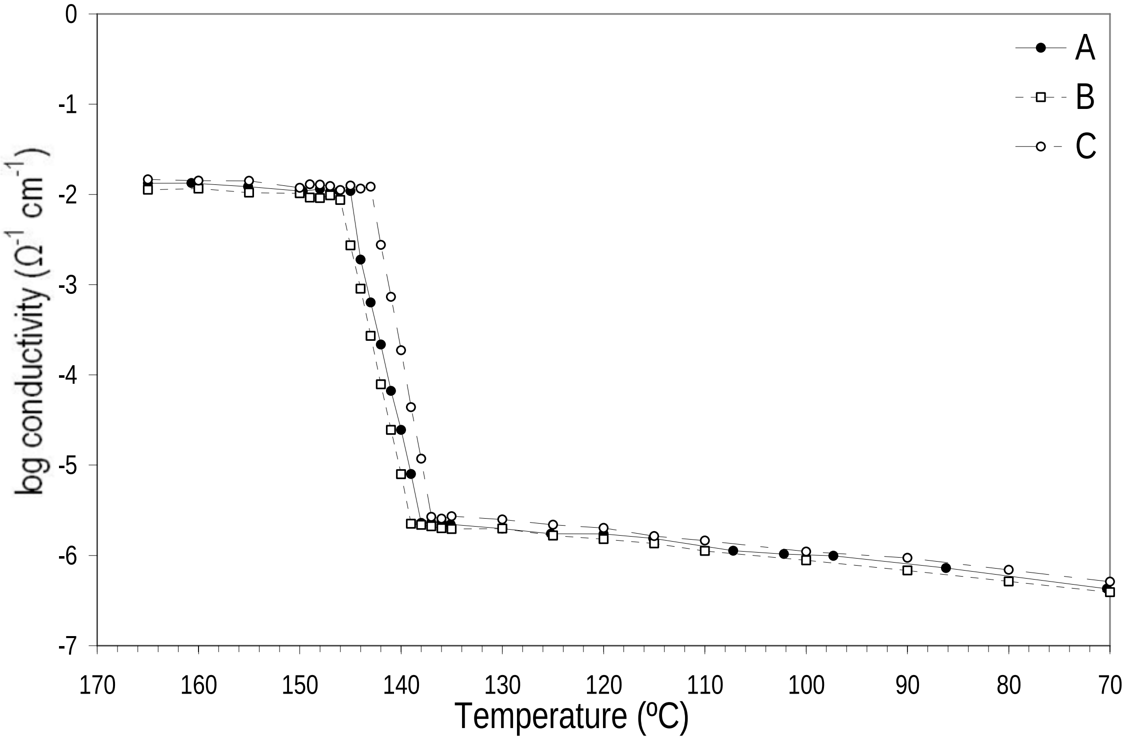

Figure 2.2 Impedance Spectra of $CsHSO_4$
Impedance spectra of $CsHSO_4$ under different preparation conditions from ferroelectric $CsHSO_4$-II phase (low temperature) to superprotonic $CsHSO_4$-I phase (high temperature). Samples shown are $CsHSO_4$ crystallized from solution by acetone (A), crystallized from solution by temperature variation (B), and crystallized by acetone, then pressed at high temperature (150 °C) (C).

Figure 2.3 shows just the high temperature, superprotonic area of the above figure.

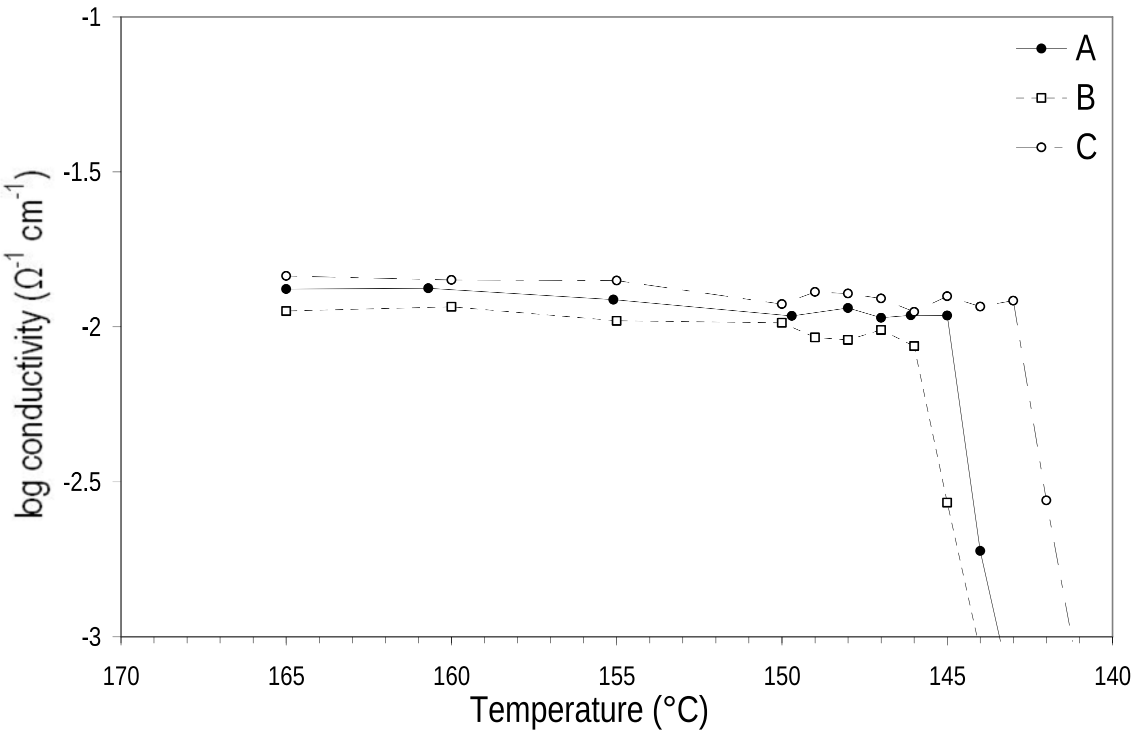

Figure 2.3 High Temperature Impedance Spectra of $CsHSO_4$
Impedance spectra of $CsHSO_4$ showing superprotonic $CsHSO_4$-I phase (high temperature) only. Samples shown are $CsHSO_4$ crystallized from solution by acetone (A), crystallized from solution by temperature variation (B), and crystallized by acetone, then pressed at high temperature (150 °C) (C).

Proton conductivities at high temperature, activation enthalpies for conduction, and pre-exponential factors all showed little variation based on synthesis and pressing method. These values are summarized in Table 2-1 below.

Table 2-1 Impedance Spectroscopy Data for $CsHSO_4$

Sample	Superprotonic Transition Temperature Range (°C)	Proton Conductivity at 150 °C (S/cm)	Activation Enthalpy for Conduction (eV)	Pre-exponential Factor (SK/cm)
A	138 to 145	0.0106	0.227	2350
B	139 to 146	0.0094	0.239	2900
C	137 to 143	0.0126	0.229	2840

2.3 Thermal Analysis

To further test their high temperature properties and verify their identity, electrolyte samples were examined using differential scanning calorimetry (DSC) and thermal gravimetric analysis (TGA). This data was used to determine the temperature at which the $CsHSO_4$ underwent transition into transition into the superprotonic phase, as well as the melting temperature. DSC/TGA data also identified dehydration activity at higher temperatures, and was used to test dehydration/deliquescence activity under a humid gas stream.

DSC uses measurements of the heat loss or gain of the sample chamber as the sample as heated. The heat into the chamber is controlled so that a constant ramp rate of the temperature is maintained. If the sample undergoes an endothermic transition, such as a phase change, this appears as a peak on the DSC spectrum. The location of that peak serves as a marker for the temperature at which that phase change occurs. In addition, by integrating beneath the peak the standard enthalpy of that transition can be determined. Ramp rates change the accuracy of these measurements, with slower ramp rates yielding more accurate results.

TGA measures the mass of the sample as the temperature is increased. A phase change from solid to superprotonic solid, or from solid to liquid, should show no change in a TGA spectrum. A change from liquid to gas, or deliquescence of the sample, should appear as decreases or increases in the TGA plot respectively.

For this work, a TA Instruments SDT Q-600 simultaneous DSC/TGA was used to analyze the samples. Powder samples of 15 to 25 mg were placed in ceramic pans and ramped from 50 to 250 ºC at a ramp rate of 5 ºC/min. For studies of dehydration and deliquescence at high temperature, samples were held for longer periods at temperatures ranging from 170 to 200 ºC, and their changes in mass were recorded under dry air streams.

A DSC/TGA of a sample of $CsHSO_4$, crystallized by acetone, is shown in Figure 2.4 below.

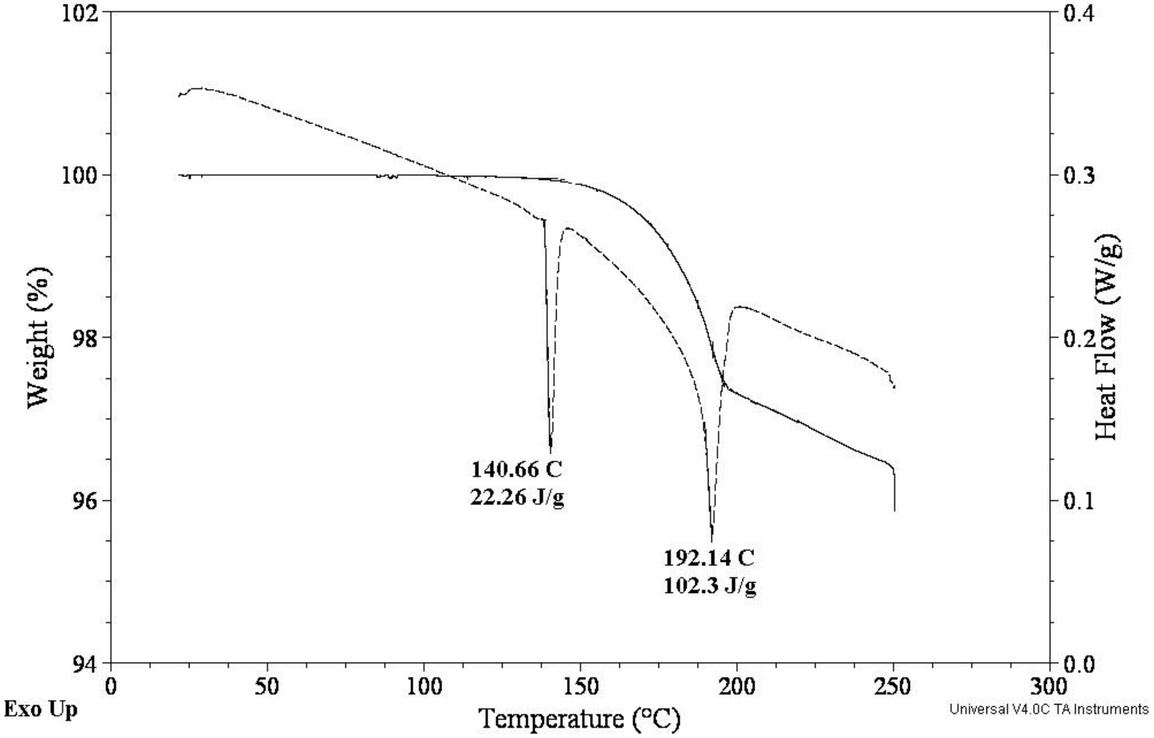

Figure 2.4 $CsHSO_4$ Crystallized by Acetone
DSC/TGA of $CsHSO_4$ crystallized by exposure to acetone. Solid line equals Weight % versus Temperature, dashed line equals Heat Flow versus Temperature. First-order solid to solid phase change at 140.66 ºC, evolution of gas (H_2O) from 162.12 ºC to 195.90 ºC.

This figure shows a sharp phase endothermic transition at 140.66 ºC, corresponding with the transition from the room temperature to the superprotonic phase. After transition to the superprotonic phase, there is a reduction in mass, also an endothermic process. This is likely the evolution of water, as the exposed sample dehydrates from $CsHSO_4$ to $Cs_2S_2O_7$. This dehydration continues until a second transition occurs at 195.90 ºC.

This same experiment was also run with $CsHSO_4$ that was crystallized by evaporation of the solvent, followed by slow chilling. The DSC/TGA profile is show in Figure 2.5.

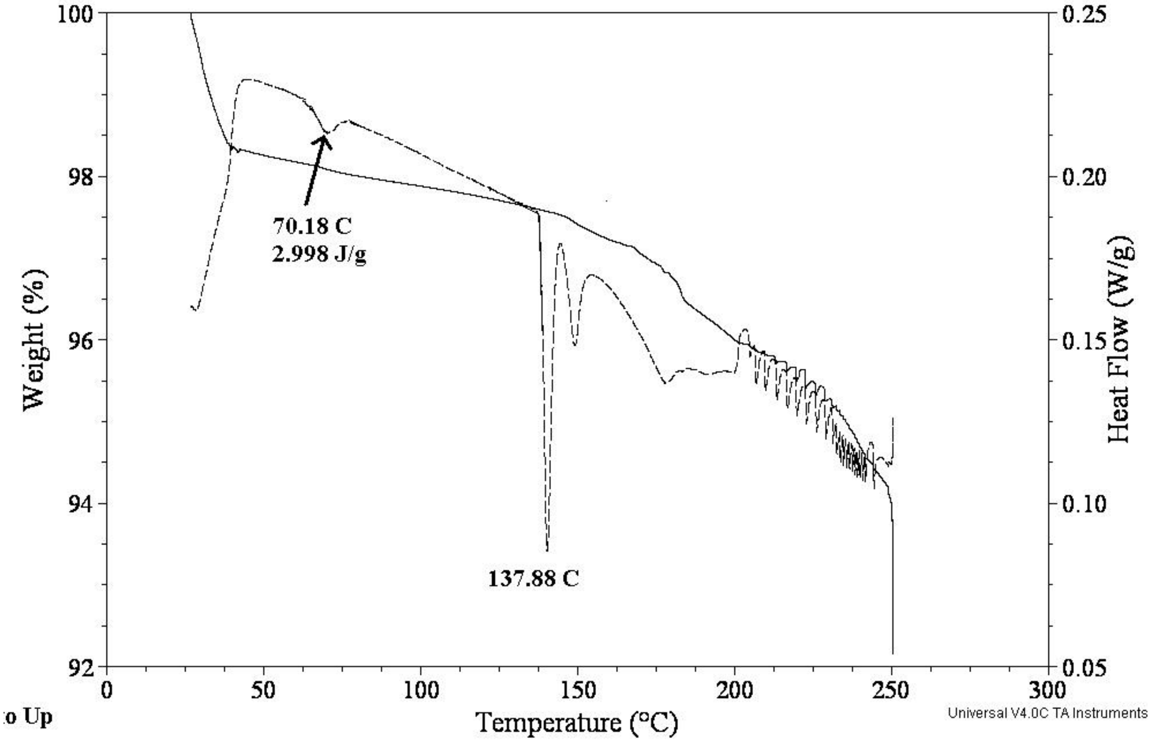

Figure 2.5 $CsHSO_4$ Crystallized by Temperature Control
DSC/TGA of $CsHSO_4$ crystallized by temperature control. Solid line indicates Weight % versus Temperature, dashed line indicates Heat Flow versus Temperature.

A sharp transition, possibly corresponding to the phase change from monoclinic to superprotonic phases, is still visible at 137.88 ºC. However, the DSC profile (heat flow versus temperature) becomes highly erratic after the transition. There is still a reduction in mass, but it is a less smooth profile. The low temperature solid-solid transition is visible on this profile at 70.18 ºC.

To verify the result show in Figure 2.5, other samples of $CsHSO_4$ that were crystallized by temperature control were examined using DSC/TGA. The results were all similar, with an erratic DSC profile after the superprotonic transition. Another example of this profile is shown in Figure 2.6.

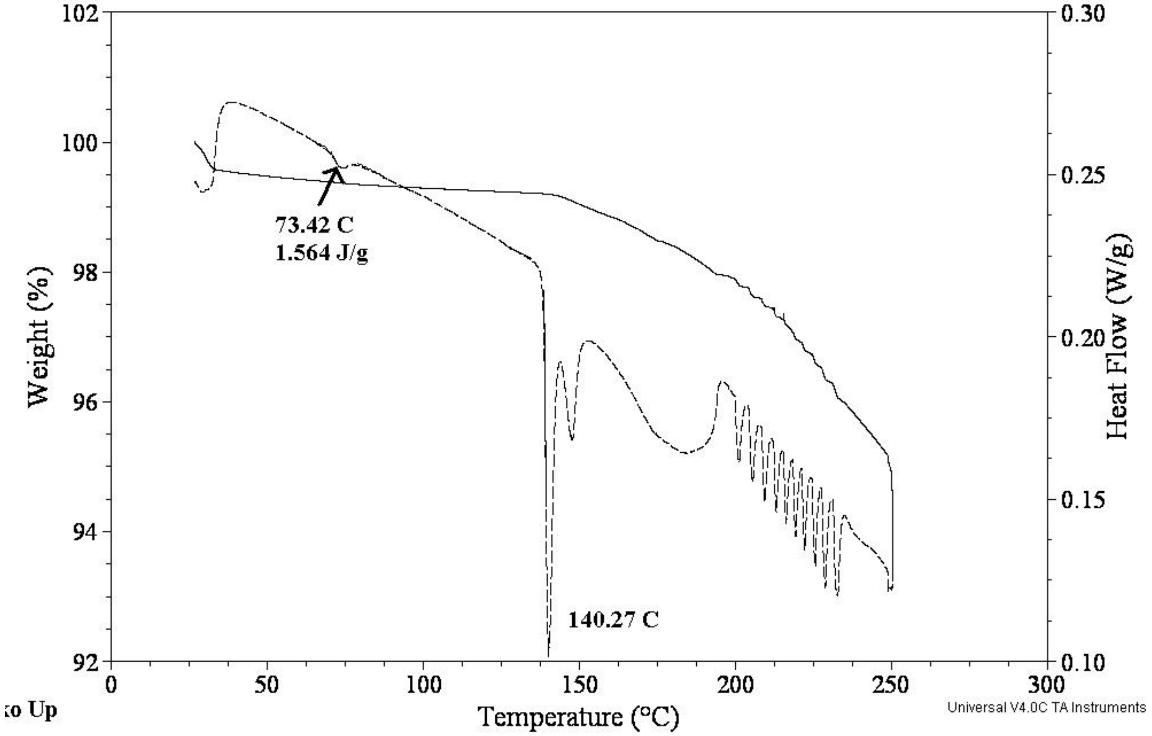

Figure 2.6 $CSHSO_4$ Crystallized by Temperature Control, a Second Attempt
DSC/TGA of $CsHSO_4$ crystallized by temperature control. The solid line indicates Weight % versus Temperature, dashed line Heat Flow versus Temperature.

The reduction in mass is still evident, but is follows a rougher profile. The DSC profile becomes erratic after the superprotonic transition. The temperature at which the transition occurs is slightly higher in this run, at 138.60 ºC, but still lower than what was observed with samples that had been crystallized using methanol or acetone. The exact temperature at which the transition occurred varied in samples that were crystallized by temperature control by ± 2 ºC.

To mitigate the effects of dehydration of the sample, $CsHSO_4$ was also analyzed using a TA Instruments Q-10 DSC, with a sealable cup and controlled atmosphere sample area. Only a limited number of runs could be performed with this instrument, because of concerns of H_2SO_4 in the sample damaging the equipment. This tool is not equipped with TGA capabilities, further limiting the direct usefulness in tracking moisture losses. A sample DSC profile taken with $CsHSO_4$ crystallized by acetone is shown in Figure 2.7.

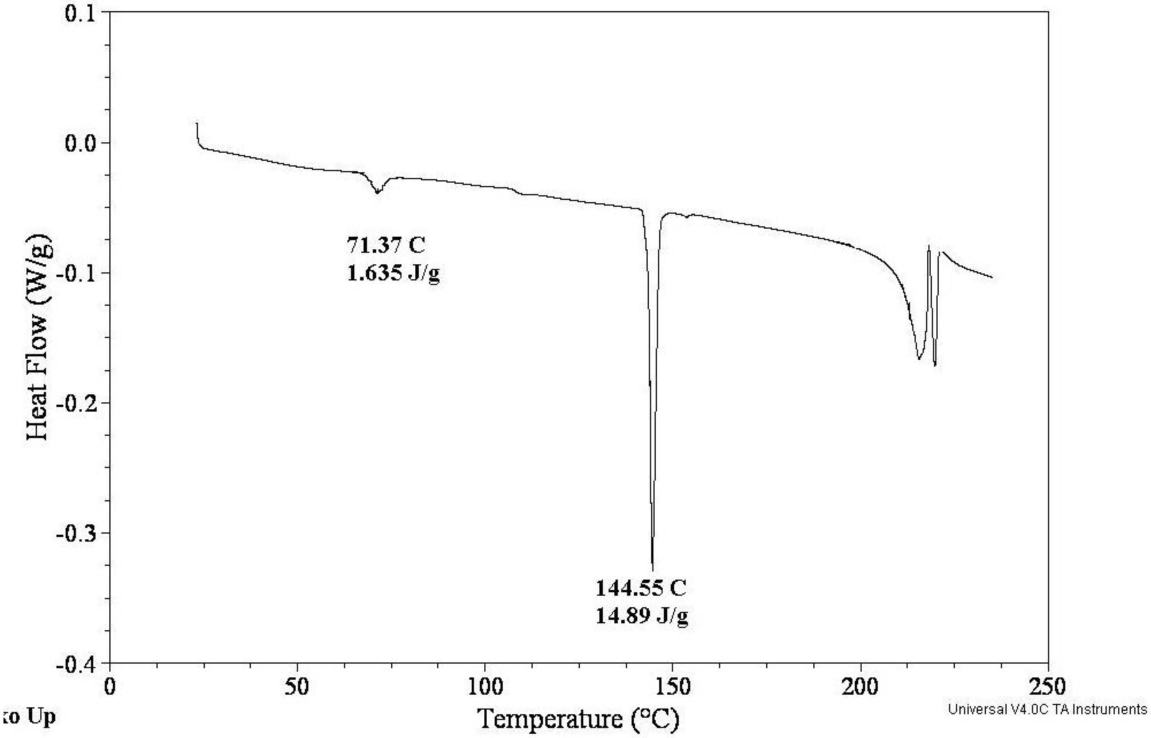

Figure 2.7 DSC of $CsHSO_4$ Using Closed Cup Q10 DSC
DSC of $CsHSO_4$ using TA Instruments Q-10 DSC with a closed cup to prevent dehydration effects.

The low temperature solid-solid transition is visible from the two monoclinic phases at 71.37 ºC, as well as the superprotonic transition at 144.55 ºC. The peak observed for the dehydration of water is not visible, most likely an indicator that water is not evolved due to the closed cup. An erratic peak is shown at 208.98 ºC. This could be due either to the rapid formation of a liquid phase, or, more likely, the pressure buildup within the closed cup of evolved water finding release, thus allowing the rapid evolution of water.

To verify that the evolution of water from the sample was producing the effects observed in the superprotonic phase, several attempts were made to produce DSC profiles of $Cs_2S_2O_7$. The first of these was excessive drying of $CsHSO_4$ in an oven at 170 ºC, followed immediately by a DSC run. The resulting profile is shown in Figure 2.8.

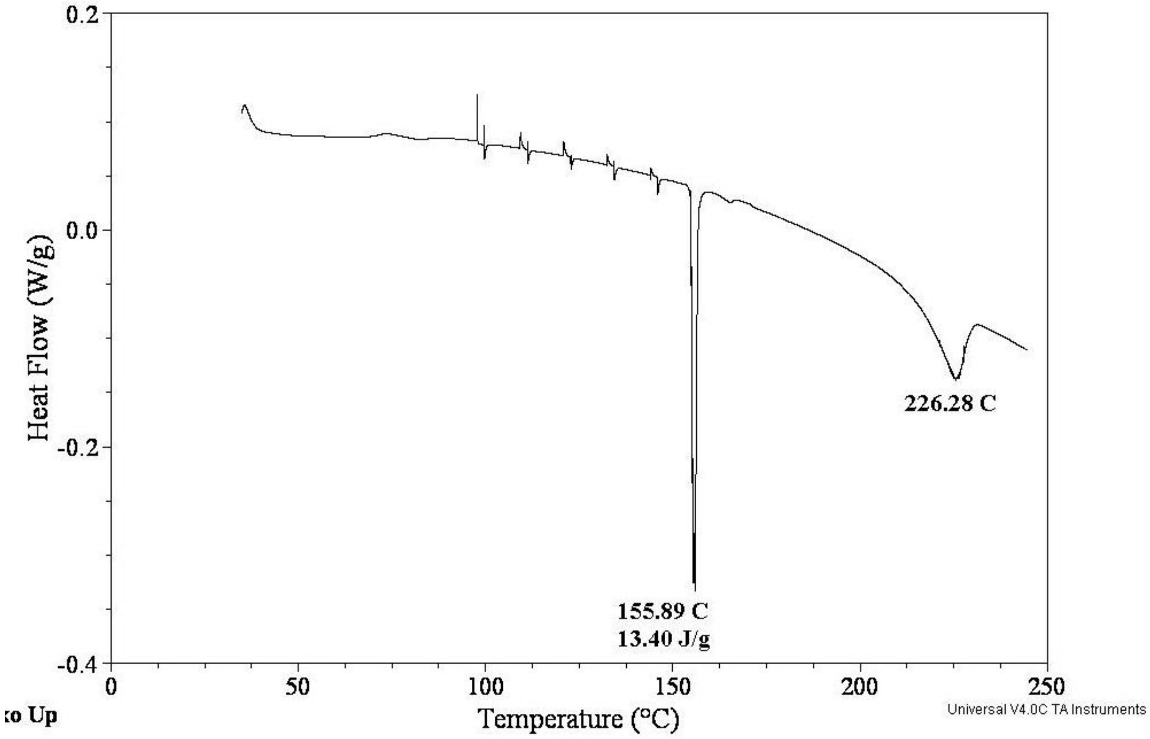

Figure 2.8 DSC of $CsHSO_4$ after Excessive Drying
DSC of $CsHSO_4$ after excessively dried at 170 ºC to determine the formation of $Cs_2S_2O_7$.

This profile still shows elements of the $CsHSO_4$ profile, leading to suspicions that the $Cs_2S_2O_7$ may have begun rehydrating back to $CsHSO_4$ while being transferred from the oven to the closed cup, reabsorbing moisture in the lab. The superprotonic transition temperature is shifted higher to 155.89 ºC, and is smaller relative to the sample size, with 13.40 J/g versus 14.89 J/g in the non-dried sample. This shift could be due to a proportion of the sample still being $Cs_2S_2O_7$ when the DSC was run. The higher temperature peak is also visible on this profile, but is shifted higher and is less erratic. If the sample contains a greater proportion of $Cs_2S_2O_7$, this can be explained as less available water to evolve from the sample, delaying the breaching of the closed cup and the rapid evolution of moisture.

Another attempt to observe the DSC profile for $Cs_2S_2O_7$ was made using the Q-600 DSC/TGA. A sample of $CsHSO_4$ was subjected to the standard ramp of temperature to determine its DSC/TGA profile. It was then quickly cooled and subjected to the rise in temperature without removing it from the tool. The resulting profile is shown in Figure 2.9.

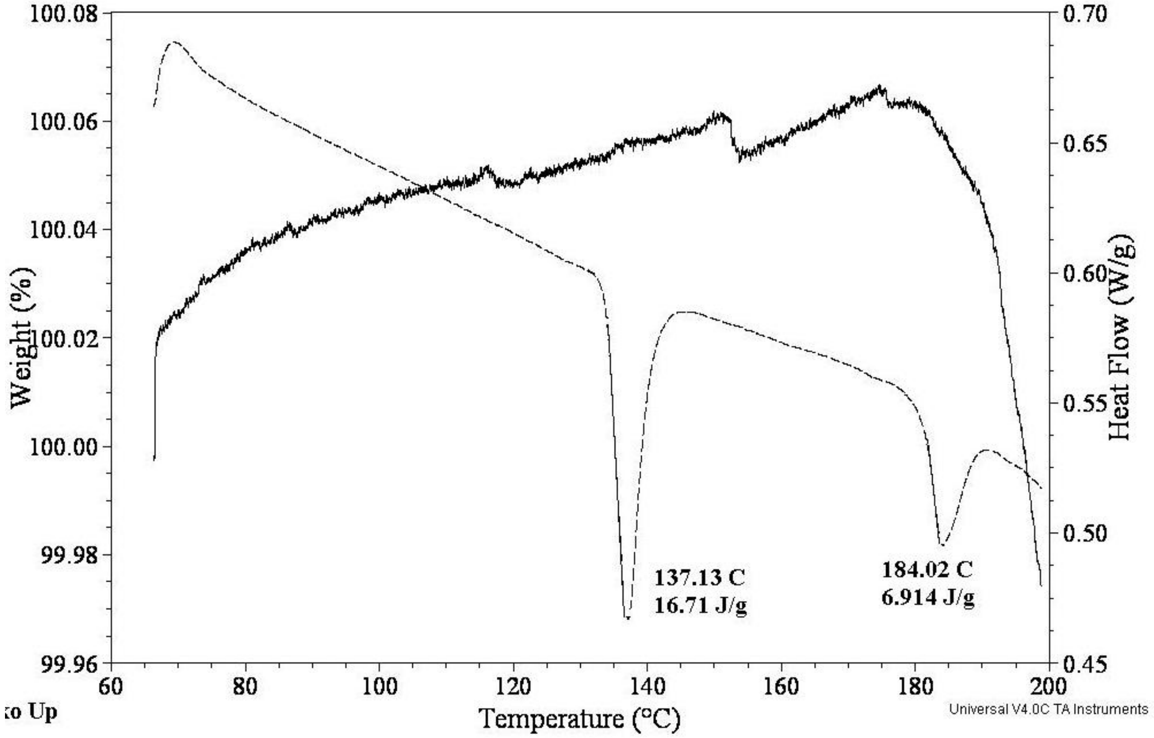

Figure 2.9 DSC/TGA of $CsHSO_4$ Rerun
DSC/TGA of $CsHSO_4$ run immediately after previous run, but without removing sample from instrument.

There is no serious weight loss associated with the evolution of water in this sample. The weight of the sample varies with ±0.02 % over the length of the run, likely due to vibrations in the sample arms because of the rapid cooling and heating. Two peaks are still visible, as in the sample of the vigorously dried sample (Figure 2.8), but are at lower temperatures. A steady, though slight, drop in the weight of the sample associated with the higher temperature suggests that it is still the evolution of water.

Transition temperatures, heats of transitions, and mass losses associated with the high temperature phase are summarized in Table 2-2 below.

Table 2-2 DSC/TGA Data for $CsHSO_4$

Sample Type	Low Temperature Transition		Superprotonic Transition		Mass Loss After SP Transition (%)	High Temperature Transition	
	Temperature (°C)	Heat (J/g)	Temperature (°C)	Heat (J/g)		Temperature (°C)	Heat (J/g)
Crystallized by Acetone	Not Observed		140.66	22.66	2.7	192.14	102.3
Crystallized by Temperature Control	70.18 73.42	2.998 1.564	137.88 140.27	Unable to Determine	4.1 4.5	Not Observed	
Crystallized by Acetone, Closed Cup	71.37	1.635	144.55	14.89	Not Measured	Not Observed	
Excessive Drying	Not Observed		155.89	13.40	Not Measured	226.28	
Run Immediately After Previous Run	Not Observed		137.13	16.71		184.02	6.914

Several long-term runs were made with $CsHSO_4$ in the TGA to determine the average amount of weight loss and the rate at which it is lost. These are shown in Figure 2.10.

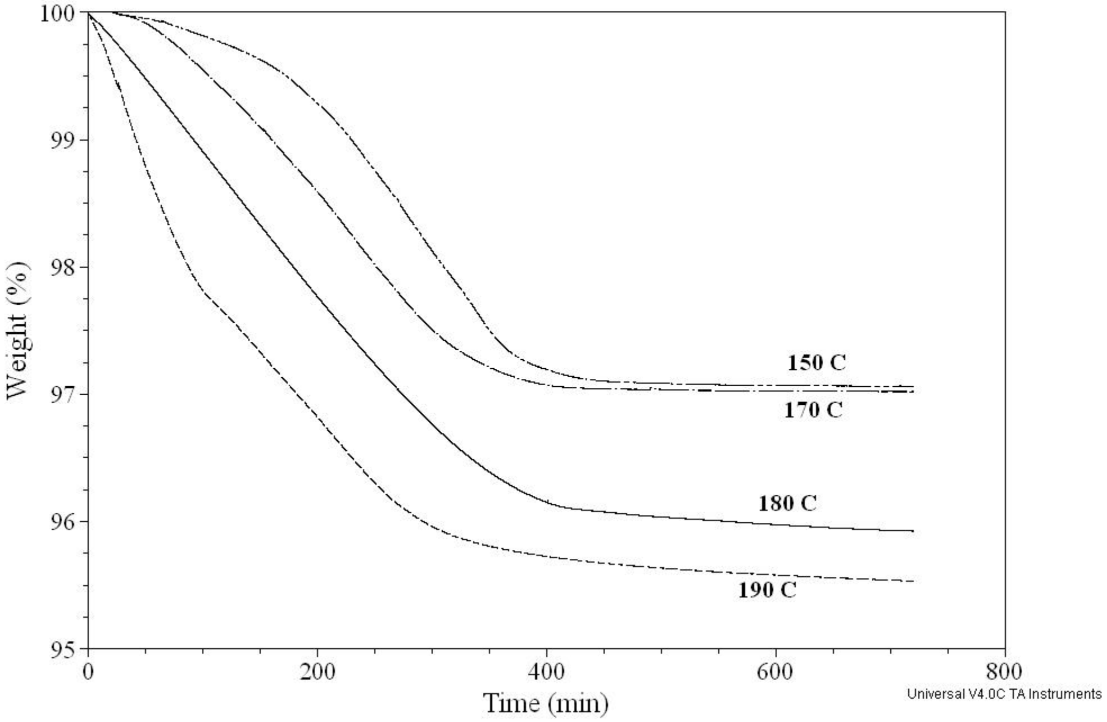

Figure 2.10 Stability of $CsHSO_4$
Weight losses of $CsHSO_4$ kept at constant temperatures to show relative degree of dehydration.

The weight loss, time to steady state, and maximum rate of weight loss associated with these four temperatures are summarized in Table 2-3 below.

Table 2-3 Data for Thermal Stability of $CsHSO_4$

Temperature (°C)	Weight Loss (%)	Time at Weight Loss Stability (minutes)	Maximum Rate of Weight Loss (%/minute)
150	2.81	450	0.013
170	2.88	420	0.011
180	3.96	410	0.013
190	4.31	350	0.027

The weight loss of all the samples was 3 to 4 %. This corresponds to the complete dissociation of $CsHSO_4$ into $Cs_2S_2O_7$ through the evolution of water.

$$CsHSO_4 = 230 \, {}^{g}\!/_{mol}$$

$$Cs_2S_2O_7 = 442 \, {}^{g}\!/_{mol}$$

$$\frac{442 \, {}^{g}\!/_{mol}}{2 \times 230 \, {}^{g}\!/_{mol}} = 0.961$$

Total dissociation of water from $CsHSO_4$ should cause a 3.9% reduction in mass.

2.4 X-ray Diffraction

The atomic structure of electrolyte produced for this work was verified using powder X-ray diffraction (XRD). By observing the diffraction pattern created from an X-ray beam striking the sample, information about the relative position of atoms in the lattice can be determined. This information allows for the identification of phases present from different synthesis methods. In addition, the width of peaks observed in an XRD pattern allows for a determination of crystallite size.

Powder X-ray diffraction techniques allow for the analysis of structural formation and phase identification of samples which do not exist as single crystals[29, 30]. A polycrystalline sample, such as the $CsHSO_4$ samples synthesized in this work, are formed of small granules or flakes, further composed of randomly oriented crystallites. An incident X-ray beam would therefore encounter crystallites in all possible three-dimensional rotations, and would diffract across all possible *hkl* planes simultaneously. This produces multiple cone shaped diffractions from a given incident angle. As the sample rotates, these cone-shaped diffractions do not change, as at any given angle from the source, the sample appears the same, as a collection of randomly oriented planes. However, the detector still passes through these diffracted cones in sequence, producing a diffraction pattern identical to that observed with single-crystal diffraction methods.

For this work, a Philips X'Pert PRO diffractometer with Cu Kα radiation (1.5418 Å) was used to probe the samples. Applied voltage and current were 45 kV and 40 mA. ½" pellets created were mounted unto the sample stage, or powder samples were placed in sample holders using a "backloading" technique. Early samples were scanned over range of $2\theta = 0$ to 90 degrees, with a scan rate of 2.4 degrees/minute. Later samples were probed over a narrower range of $2\theta = 10$ to 50 degrees, with a scan rate of 1.2 degrees/minute. The data was analyzed using Phillips X'Pert Highscore and the Inorganic Crystal Structure Database and the International Centre for Diffraction Data.

Figure 2.11 shows an experimental pattern from $CsHSO_4$ powder crystallized by acetone. Also shown is a reference pattern[31] for $CsHSO_4$-III showing a strong match to the experimental pattern.

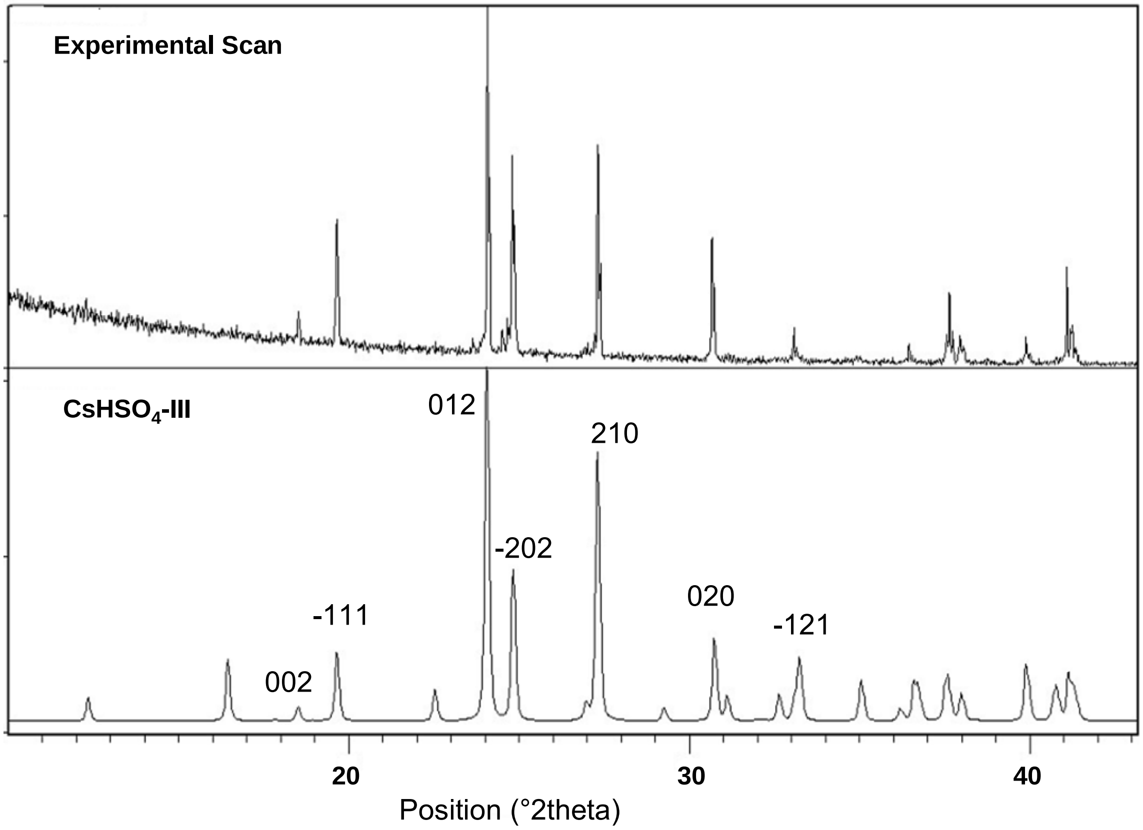

Figure 2.11 PXRD Pattern of Monoclinic $CsHSO_4$-III
Experimental PXRD pattern of $CsHSO_4$ (top) and reference pattern of $CsHSO_4$-III ($P2_1/n$) (bottom) showing solid correlation between peaks in PXRD versus peaks from single crystal.

Dominant peaks in the experimental pattern and their most likely matches from the reference pattern are shown in Table 2-4 below.

Table 2-4 Experimental PXRD versus $CsHSO_4$-III Reference Pattern
Comparison of peaks observed in experimental pattern to those from $CsHSO_4$-III reference pattern[31], showing strong correlation.

Experimental Pattern (°2θ)	$CsHSO_4$-III Reference Pattern			
	Position (°2θ)	h	k	l
18.509	18.496	0	0	2
19.650	19.637	-1	1	1
24.071	24.039	0	1	2
24.811	24.813	-2	0	2
27.312	27.290	2	1	0
30.670	30.719	0	2	0
33.071	33.220	-1	2	1

An experimental pattern of $CsHSO_4$ crystallized by methanol is shown in Figure 2.12 below. This pattern showed features of $CsHSO_4$-III and $CsHSO_4$-II reference patterns, as shown in the figure.

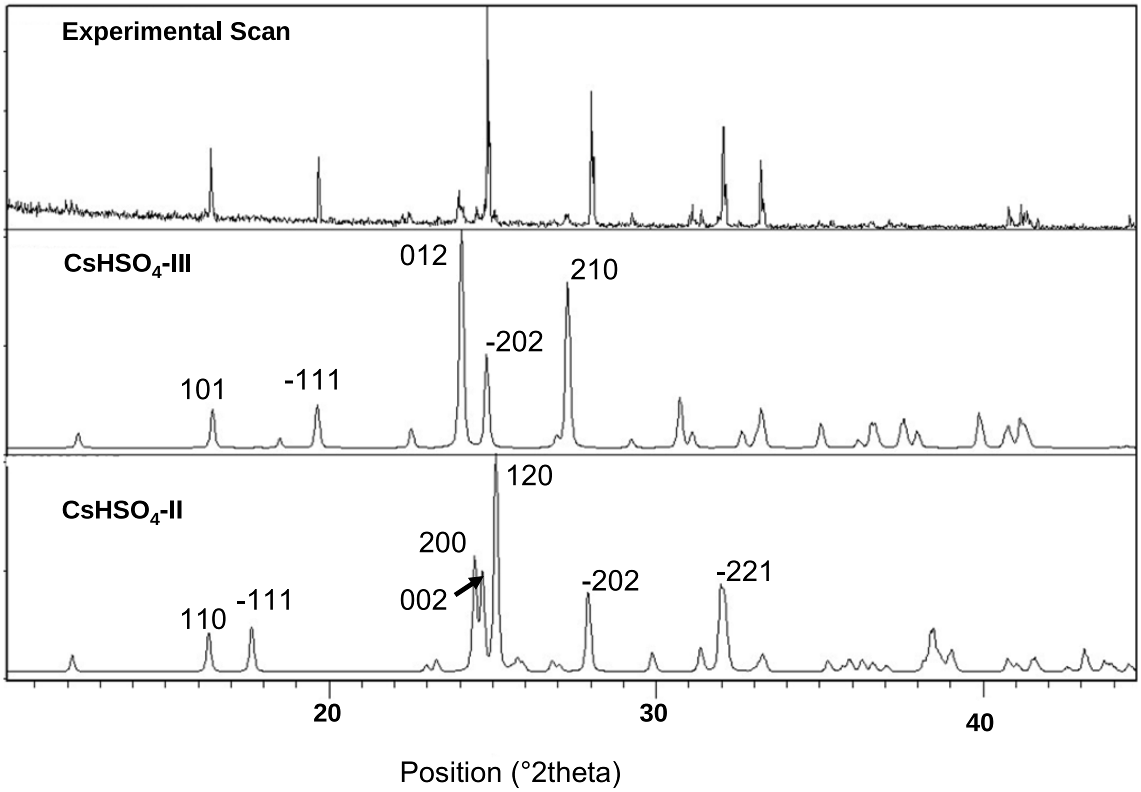

Figure 2.12 PXRD of $CsHSO_4$ Showing $CsHSO_4$-II and $CsHSO_4$-III Features
Experimental PXRD pattern of $CsHSO_4$ (top), reference pattern of $CsHSO_4$-III ($P2_1/n$) (middle), and reference pattern of $CsHSO_4$-II ($P2_1/c$) (bottom) showing a mix of features from reference scans found in experimental pattern.

Strong peaks from the experimental pattern along with likely candidates from both reference patterns are shown in Table 2-5 below.

Table 2-5 Experimental PXRD versus CsHSO$_4$-III and CsHSO$_4$-II Reference Patterns Comparison of peaks observed in experimental pattern to those from CsHSO$_4$-III and CsHSO$_4$-II reference patterns[31], showing elements of both reference materials in experimental sample.

Experimental Pattern (°2θ)	CsHSO$_4$-III Reference Pattern				CsHSO$_4$-II Reference Pattern			
	Position (°2θ)	h	k	l	Position (°2θ)	h	k	l
16.390	16.435	1	0	1	16.321	1	1	0
					17.634	-1	1	1
19.691	19.637	-1	1	1				
	24.039	0	1	2				
					24.445	2	0	0
					24.680	0	0	2
24.855	24.813	-2	0	2	25.094	1	2	0
	27.290	2	1	0				
28.031					27.920	-2	0	2
32.064					31.977	-2	2	1
33.211								

A sample of CsHSO$_4$ was excessively dried in an oven overnight, to determine the effect of the drying step on electrolyte structure. The PXRD pattern is shown in Figure 2.13, along with the reference pattern for CsHSO$_4$-II.

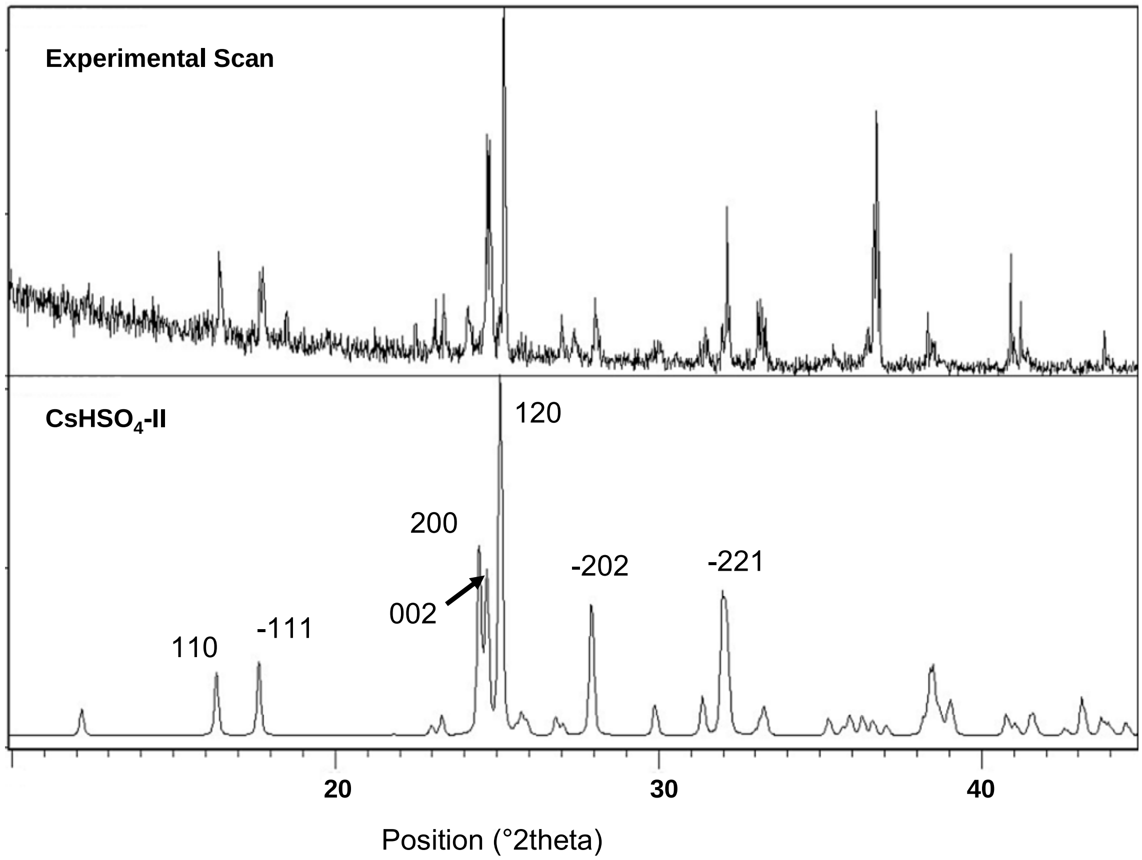

Figure 2.13 PXRD Pattern of Monoclinic $CsHSO_4$-II
Experimental PXRD pattern of $CsHSO_4$ (top) and reference pattern of $CsHSO_4$-II ($P2_1/c$) (bottom) showing solid correlation between peaks in PXRD versus peaks from single crystal.

The strong peaks from this experimental scan are matched with the most likely candidates from the $CsHSO_4$-II reference pattern in Table 2-6 below.

Table 2-6 Experimental PXRD versus $CsHSO_4$-II Reference Pattern
Comparison of peaks observed in experimental pattern to those from $CsHSO_4$-II reference pattern[31], showing strong correlation.

Experimental Pattern (°2θ)	$CsHSO_4$-II Reference Pattern			
	Position (°2θ)	h	k	l
16.412	16.321	1	1	0
17.672	17.634	-1	1	1
24.711	24.445	2	0	0
24.790	24.680	0	0	2
25.230	25.094	1	2	0
32.132	31.977	-2	2	1

Crystallite size can be estimated from the width of the peaks observed in the diffraction pattern[30]. For a given peak, Bragg's Law must be satisfied for the crystal spacing, wavelength of incident light, and angle at which the beam strikes the crystal plane:

$$\lambda = 2d \sin \theta_B$$

where , λ is the wavelength of the incident X-ray beam, d is the spacing between crystal planes, and θ_B is angle which satisfies Bragg's Law for the given d and λ. (note that typically XRD patterns are shown as intensity versus $2\theta_B$).

For a given peak, the full width at half maximum can be approximated by assuming the peak's shape as a triangle.

$$B = \frac{1}{2}(2\theta_1 - 2\theta_2) = \theta_1 - \theta_2$$

where B is the full width at half max, and $2\theta_1$ and $2\theta_2$ are the endpoints of the peak observed on the pattern.

Bragg's Law can be applied to the two angles at the endpoints of the peak, assuming a number of crystal layers m:

$$\begin{aligned} 2t \sin \theta_1 &= (m+1)\lambda \\ 2t \sin \theta_2 &= (m-1)\lambda \end{aligned}$$

Where t is the total thickness of the crystallite, t = md.

Approximating:

$$\theta_1 + \theta_2 = 2\theta_B \text{ and } \sin\left(\frac{\theta_1 - \theta_2}{2}\right) = \left(\frac{\theta_1 - \theta_2}{2}\right)$$

Then solving for t results in:

$$t = \frac{K\lambda}{B\cos\theta_B}$$

where K is a correction factor based on the assumed shapes of the crystallites. Values of K vary from 0.7 to 1.05, and are unitless quantities. For this work, a shape factor of 0.9 associated with parallel planes was used.

Table 2-7 shows calculated crystal sizes from the three samples shown in Figures 2.11 to 2.13, as well as crystallite sizes calculated for $CsHSO_4$ crystallized by temperature control. Samples crystallized by temperature control produced peaks, but did not match any reference pattern for $CsHSO_4$.

Table 2-7 $CsHSO_4$ Crystallite Size

$CsHSO_4$ crystallite sizes calculated from PXRD data using Sherrer's Formula.

	Phase	Average Crystallite Size (Å)	Standard Deviation (Å)
Sample A (Acetone)	$CsHSO_4$-III	3308	621
Sample B (Methanol)	$CsHSO_4$-III and $CsHSO_4$-II	3748	316
Sample C (Excessively Dried)	$CsHSO_4$-II	2997	838
Sample D (temp control)	Unknown	4228	692

Crystallite sizes ranged from approximately 3000 to 4200 Å, with larger crystallites associated with crystallization using temperature control. Crystallization using methanol yielded crystallites larger than those yielded by acetone crystallization.

2.5 X-ray Photoelectron Spectroscopy

X-ray photoelectron spectroscopy (XPS) was used to probe the surface atoms of $CsHSO_4$ powders and pellets, to determine the presence or absence of absorbed species, particularly alcohols left over from the crystallization or sintering steps.

When an atom is struck by an X-ray, a photoelectron may be ejected. This electron will have a kinetic energy equal to the difference between the energy of the X-ray photon that struck it, and the binding energy required to excite the electron from its bound orbital state to a free electron[32, 33].

In addition, electrons in higher orbitals may relax down to orbitals vacated by electrons. The difference in energy is transferred to a neighboring electron, which is emitted with a kinetic energy equal to the difference between the change in binding energy experienced by the relaxing electron and the binding energy of the electron emitted.

XPS can also determine the chemical state of an atom. Forming molecular bonds changes the binding energy of electrons in an atom, resulting in a shift in the kinetic energy observed for emitted photoelectrons.

XPS data for this work was obtained using a Perkin-Elmer PHI 560 ESCA/SAM system, operated at approximately 5 x 10^{-10} Torr. The X-ray source was a magnesium filament in a PHI 04-500 dual X-ray source, with a voltage of 15 kV and a current of 20 mA. For survey scans, a pass energy of 100 eV was used, while a 50 eV pass energy was used for high resolution scans. The kinetic energy of emitted electrons was measured using a 25-270AR cylindrical mirror analyzer, while the data was analyzed using AugerScan.

From a $CsHSO_4$ sample we would expect to see peaks associated with the binding energies of Cs, S, and O, as well as carbon that has formed on the surface of the sample from the lab. Expected binding energies for these species, as well as atomic sensitivity factors for selected peaks, are shown in Table 2-8.

Table 2-8 Binding Energies and Atomic Sensitivity Factors for Species Present in $CsHSO_4$[34]

Element	Atomic Shell	Binding Energy (eV)	Atomic Sensitivity Factor
Cs	3s	1219	
Cs	$3p_{1/2}$	1069	
Cs	$3p_{3/2}$	1002	
Cs	$3d_{3/2}$	740	
Cs	$3d_{5/2}$	726	7.041
O	1s	531	0.711
C	1s	285	0.296
Cs	4s	234	
S	2s	228	
Cs	$4p_{1/2}$	173	
S	$2p_{1/2}$	165	
S	$2p_{3/2}$	164	0.666
Cs	$4p_{3/2}$	161	
Cs	$4d_{3/2}$	80	
Cs	$4d_{5/2}$	77	
Cs	5s	25	
O	2s	23	
S	3s	18	

A typical XPS survey scan for $CsHSO_4$ is shown in Figure 2.14. This sample was crystallized by added methanol to solution.

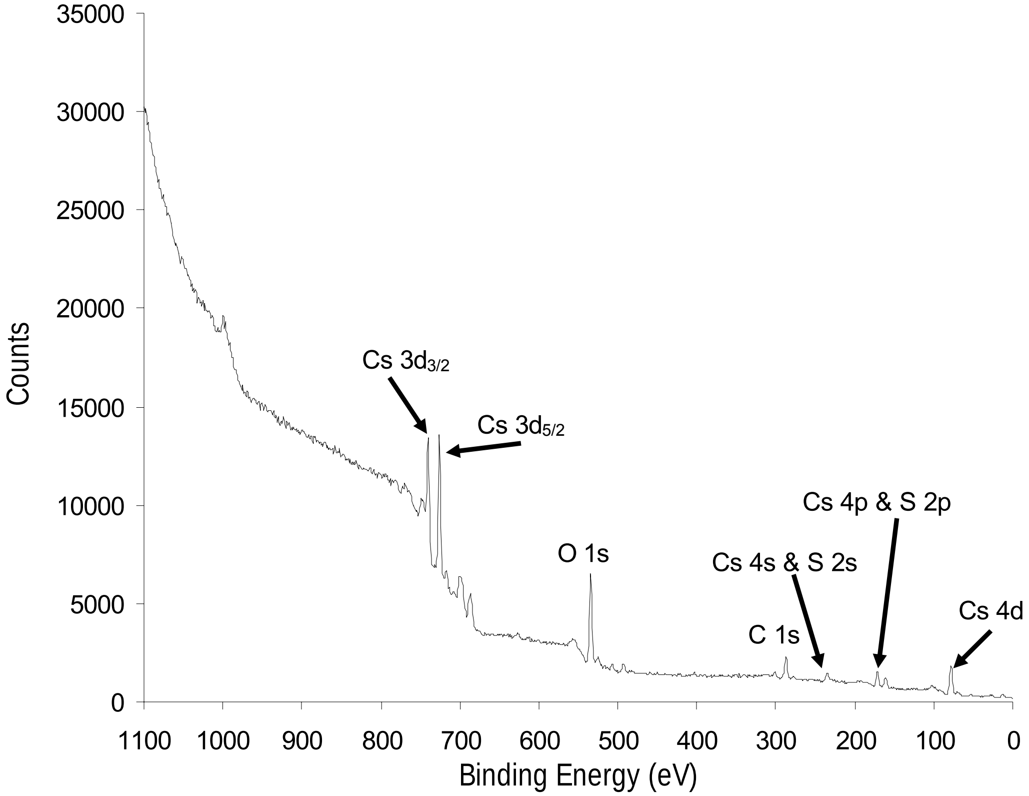

Figure 2.14 X-ray Photoelectron Spectroscopy Survey Scan of $CsHSO_4$ Powder Crystallized with Methanol
This is a typical survey scan of $CsHSO_4$ showing peaks associated with the binding energies of different atomic shells within the sample.

Determining atomic ratios for $CsHSO_4$ is hampered by the low atomic sensitivity of sulfur compared to that of cesium, and that characteristic sulfur peaks lie very close to cesium peaks (sulfur 2s is very close to cesium 4s, and sulfur $2p_{1/2}$ and $2p_{3/2}$ are very close to cesium $4p_{1/2}$ and $4p_{3/2}$) meaning that the cesium peaks overwhelm the sulfur peaks.

Figure 2.15 shows a high resolution scan about the cesium 4p and sulfur 2p peaks. The sulfur peaks are all but indecipherable against the larger cesium peaks.

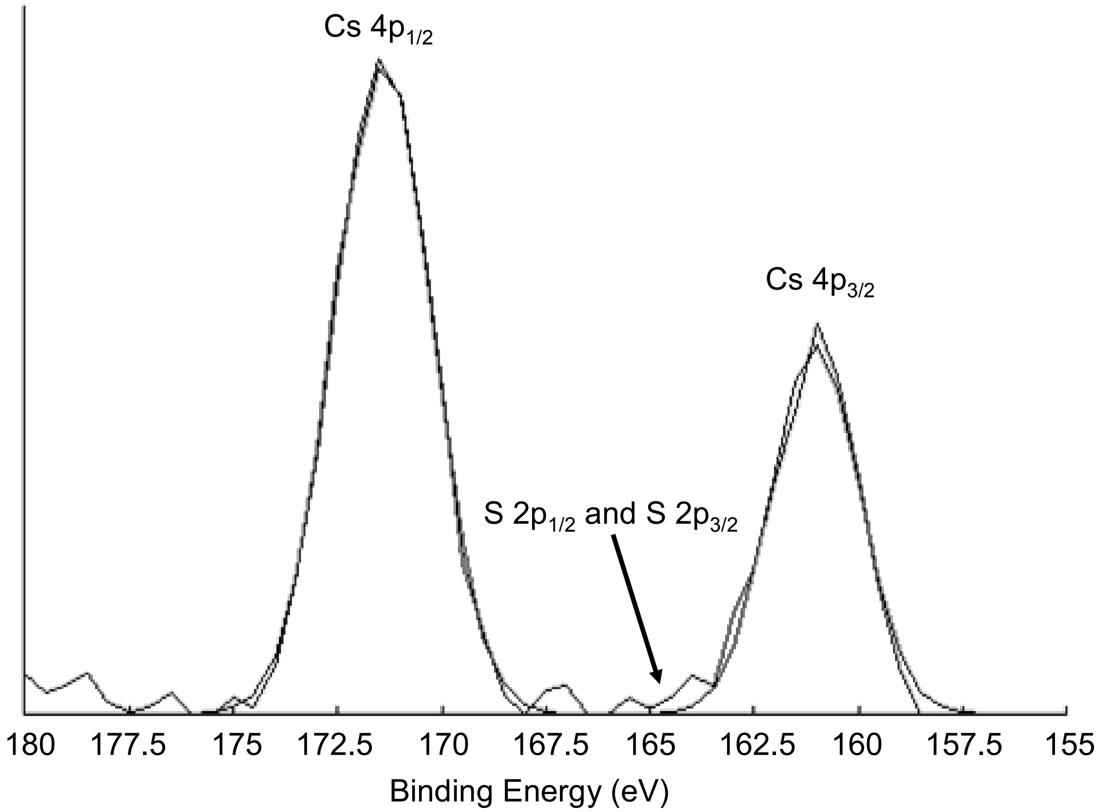

Figure 2.15 XPS High Resolution Scan of Sulfur 2p Peaks
High resolution XPS scan (background subtracted) of sulfur $2p_{1/2}$ and $2p_{3/2}$ peaks, showing their low sensitivity factor versus energetically similar cesium $4p_{1/2}$ and $4p_{3/2}$ peaks.

3 Permeability Studies

Since the electric potential and current density of a fuel cell can both be lowered by fuel or oxidant gases permeating through the electrolyte, a study of gas permeability characteristics of $CsHSO_4$ was undertaken.

3.1 Permeability

Experimentally, the flux through a membrane is typically measured directly by monitoring the concentration of the desired solute on the acceptor side of the membrane[35]. This concentration function can be derived from a basic mass balance performed on the acceptor side.

Starting with a mass balance expression:

$$\text{Flux}_{\text{in}} - \text{Flux}_{\text{out}} = \text{Accumulation}$$

The flux in the above expression includes both the flux due to diffusion across the membrane as well as flux due to the convection of solvent carrying solute through the membrane. However, the proposed experimental setup has no pressure difference across the membrane, and the volume of material on both sides of the membrane is approximately equal. Thus the flux due to convection is considered negligible.

From sources discussing the behavior of membranes, flux due to diffusion alone is shown to be[35, 36]:

$$Flux = A\frac{D \cdot K}{L}c$$

Where A is the cross-sectional area of the membrane, L is the membrane thickness, D is the diffusion coefficient for the solute between the membrane and the adjacent solution, K is the partition coefficient for the solute between the membrane and the adjacent solution, and c is the concentration providing the driving force. Combining terms back into the balance expression:

$$V_B\frac{dc_B}{dt} = A\frac{D \cdot K}{L}(c_A - c_B)$$

Where c_B is the concentration on the acceptor side of the membrane and c_A is the concentration on the donor side of the membrane.

At the operating conditions of the experiment the concentration on the acceptor side of the membrane is always negligible relative to the concentration on the donor side, so we assume c_B goes to zero on the RHS of the above equation. That is, there is negligible diffusive flux backwards across the membrane due to concentration on the acceptor side during the experiment.

$$V_B \frac{dc_B}{dt} = A \frac{D \cdot K}{L} c_A$$

Assuming the concentration on the donor side does not change during the experiment and that the initial condition for the concentration on the acceptor is zero, this equation can be solved for c_B. The following expression is the result:

$$c_B(t) = \frac{A}{V_B} \frac{P}{L} c_A (t - t_0)$$

where P is the membrane permeability defined as the product D x K. This equation includes a time delay, t_0, the result of the constant of integration. This time delay is due to the initial diffusion through the membrane immediately after the addition of solute to the donor side, as well as the brief time before linearity is established on the acceptor side. This time lag is explicitly related to the diffusivity by[36]:

$$t_0 = \frac{L^2}{6D}$$

It is desirable to determine how the permeation through a membrane varies with temperature.

The permeability at a given temperature can be obtained from the slope of the curve of the concentration in the acceptor side versus time. In general, the relation between permeability of a membrane with temperature is expressed as a form of the Arrhenius Law, as shown[37]:

$$P = P_\infty \exp\left(-\frac{E_a}{RT}\right)$$

Where P_∞ is the permeability at an infinitely high temperature, E_a is the activation energy for the permeation of the given solute across the membrane, R is the gas constant, and T is absolute temperature. Taking the log of both sides results in:

$$\ln P = \ln P_\infty - \frac{E_a}{RT}$$

Thus the slope of plot of the ln P versus 1/T will have a slope equal to E_a/R, allowing one to determine the activation energy.

3.2 Experimental Setup

An experimental cell was constructed to test permeability of manufactured membranes. This cell had two chambers, separated by the membrane to be tested. Gas inlets could be regulated into and out of either chamber by means of a manifold and rotometers. The cell was kept in a convection oven to ensure even heating, while all inlet lines passed through coils within the oven to insure that inlet gases were not lowering the temperature at the surface of the membrane. Samples were removed from one of the chambers (the acceptor side) by means of an Ultra-Torr© diaphragm with a 10 μl syringe. This sample size was small enough to not cause a significant loss of gas in the acceptor side compared to the size of the chamber. Samples were then analyzed using gas chromatography (see below) to determine the concentration of the species permeating through the membrane.

Gases to be tested were fed into the donor side of the cell at 100% concentration, while nitrogen was fed into the acceptor side. This was done for thirty minutes to insure a steady-state starting condition of 100% of the test gas on the donor side and 0% on the acceptor side. Flow of nitrogen to the acceptor side was halted at time zero, when measurements were taken from the acceptor side. All valves on the acceptor side were closed, while those on the donor side remained open, so that the concentration on the donor side remained nearly constant. The flow of test gas through the donor side of the cell was kept at low values of 10 to 15 μl per minute, so that pressure differentials across the membrane could be neglected.

Figure 3.1 shows a cross-section of the permeability cell used for experimental measurements.

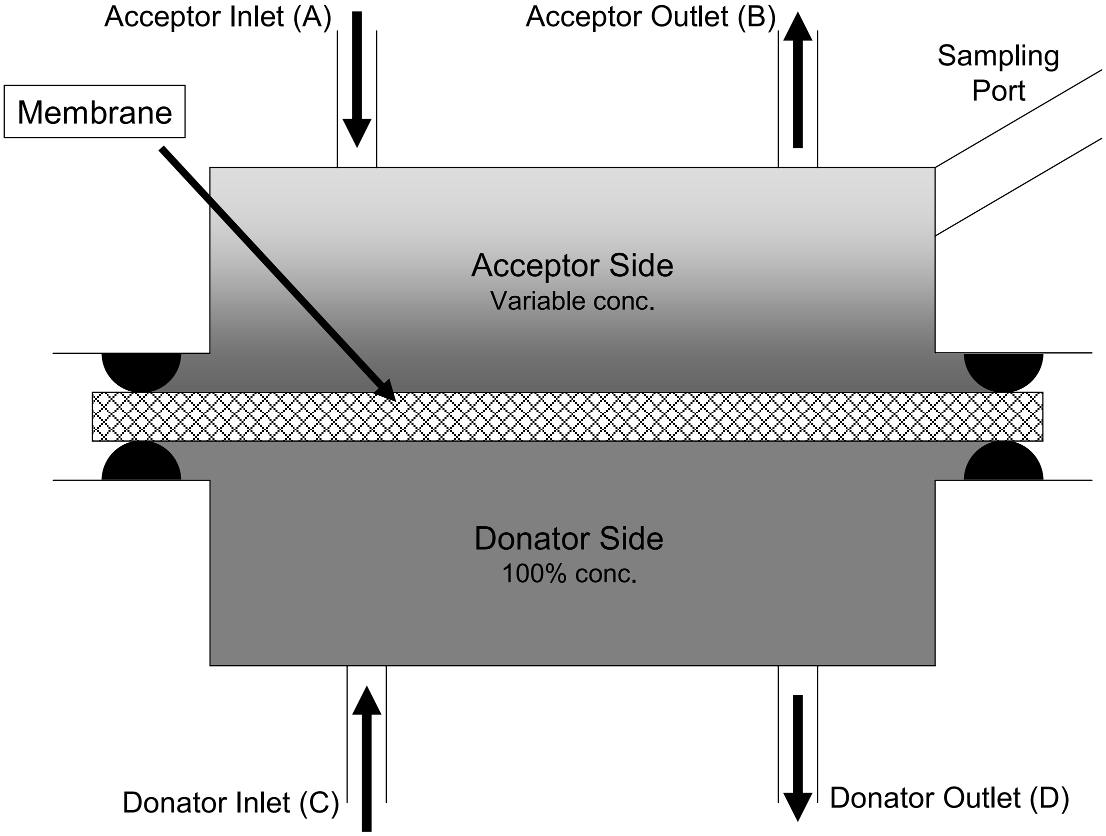

Figure 3.1 Schematic of the Permeability Cell
Cross-sectional schematic of experimental setup for permeability experiments. Gas to be tested is fed through the donator side from C to D. Nitrogen is fed through the acceptor side from A to B, until a steady state has been achieved. Then the nitrogen flow is closed off at both A and B. Samples are taken over time from the sampling port.

3.3 Gas Chromatography

Gas chromatography allowed quantitative evaluation of gases produced during electrolysis or for permeation testing of membranes[38, 39]. A gas separation was performed within the chromatograph column, and as the different species left the column, they were detected producing a signal proportional to the amount of that species. Using a calibration curve of signal strength to concentration, the makeup of the gas could be determined.

Quantitative analysis of gas species was obtained using an Agilent Technologies 6890N Network Gas Chromatograph. Gas samples were injected into one end of an HP-5 Phenyl Methyl Siloxane column (Agilent 19091J-413) 30 m long with an inner diameter of 320 µm and an average film thickness of 0.25 µm. Injection temperature was 250 ºC. Helium at 229 ml/min was used as a pass-through gas, though an oven at 40 ºC. A flame ionization detector operating at 300 ºC with a H_2 / air mix of 1:10 was used to detect gas species leaving the column. The data was analyzed using Chemstation Rev. A.10.02.

3.4 Effect of Methanol

Methanol was chosen to be the first gas investigated. Initial runs with methanol showed a steadily increasing concentration on the acceptor side with time. This concentration curve reached an upper limit, after which it did not increase. One would expect the concentration of methanol to continue increasing to 100% at some long time, but this was not the case.

Subsequent runs were attempted without changing the membrane in the permeability cell. Both sides were flushed thoroughly with nitrogen, and the same experimental procedure was followed. When this was done methanol permeation was drastically reduced versus that through a fresh pellet.

Permeation profiles versus time for fresh $CsHSO_4$ and those already subjected to the runs are shown in Figure 3.2.

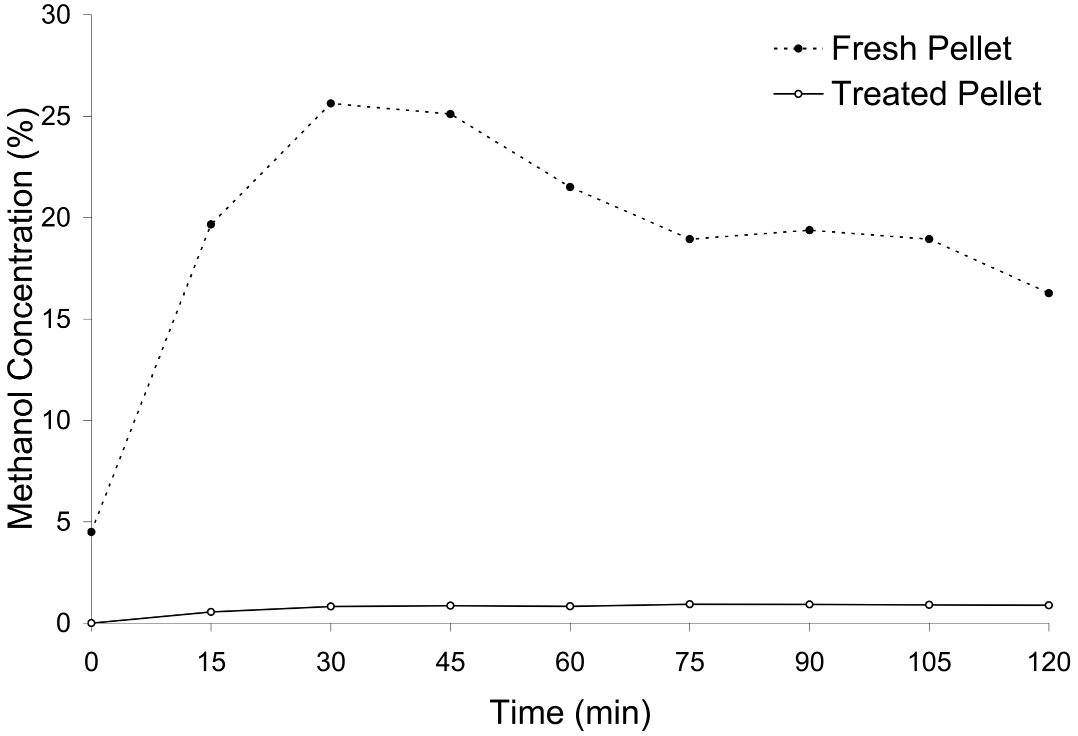

Figure 3.2 Permeation Response of $CsHSO_4$ Membrane to Methanol Vapor
Methanol concentration in the acceptor side of the permeation cell versus time for a fresh membrane of $CsHSO_4$ (black circles, dashed line) and a membrane of $CsHSO_4$ already treated with methanol permeation (white circles, solid line).

The same permeation experiment was also attempted with methane as the permeation gas. Like methanol, methane permeated freely through freshly made membranes of $CsHSO_4$. Unlike methanol, methane did not level off at as low of a value, and continued to rise throughout the length of the experiment. If the experiment was run long enough, eventually 100% methane was all that remained in the acceptor side of the cell.

Figure 3.3 shows the results of several permeation runs of methane through fresh $CsHSO_4$ membranes. Also shown is a weighted average of experimental data.

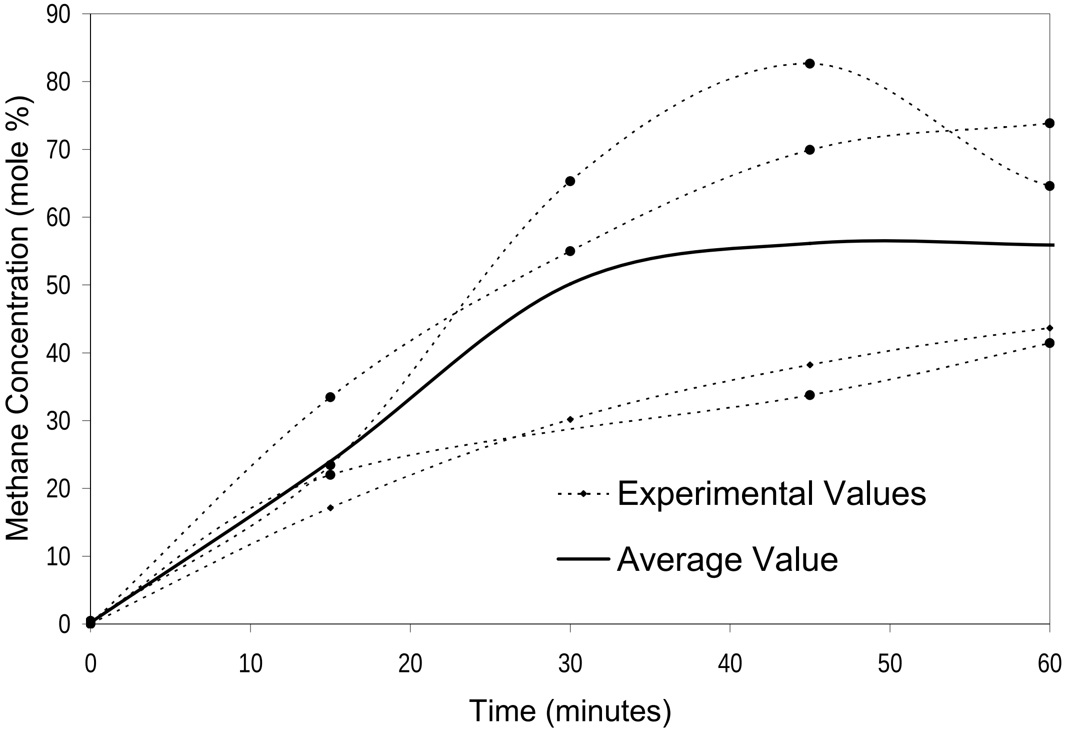

Figure 3.3 Permeation of Methane through Fresh $CsHSO_4$ Membrane
Methane concentrations in the acceptor side of the permeability cell versus time for several membranes of $CsHSO_4$ (dashed lines). The solid line is a weighted average of these profiles.

Experiments were also conducted with methane permeating through membranes that had already been treated with methanol. These profiles showed a marked decrease in the permeability of $CsHSO_4$ to methane after it had been treated with methanol. Molar flux across the membrane was decreased by nearly three full orders of magnitude after treatment with methanol.

Figure 3.4 shows the results of several permeation runs of methane across a $CsHSO_4$ membrane that had been treated with methanol.

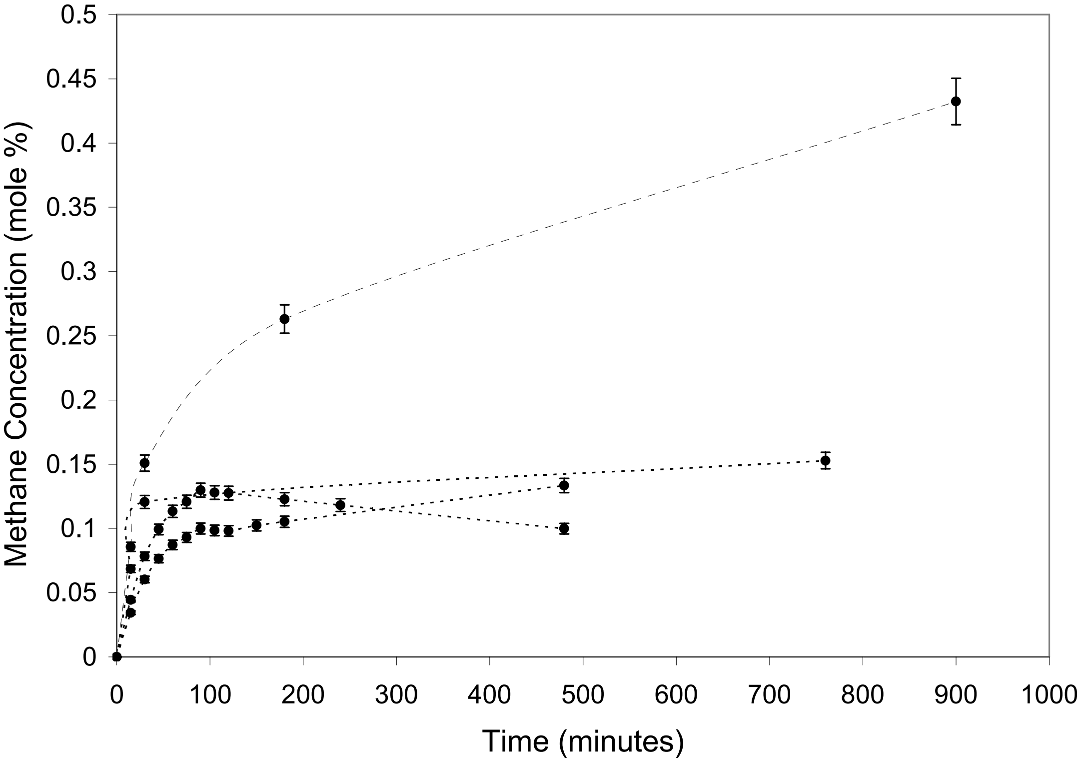

Figure 3.4 Permeation of Methane through $CsHSO_4$ Membrane after Treatment with Methanol
Methane concentrations in the acceptor side of the permeability cell versus time for several methanol-treated membranes of $CsHSO_4$.

Data for methane permeability through fresh and treated membranes of $CsHSO_4$ is shown in Table 3-1.

Table 3-1 Permeation Data for Methane through $CsHSO_4$

	Fresh Membrane	Membrane Treated with Methanol
Flux of methane across membrane for short times (gmol/(m^2s))	3.74 x 10^{-5}	4.22 x 10^{-8}
Permeability of membrane to methane (s^{-1})	1.03 x 10^{-5}	1.17 x 10^{-8}
Steady state concentration of methane	45 to 100%	0.1 to 0.5%
Time to achieve steady state value	30 to 50 minutes	100 to 300 minutes

An investigation of the interaction between a methanol-treated $CsHSO_4$ pellet and steam was also undertaken in this study. Earlier tests has shown that introducing steam into a cell containing $CsHSO_4$, even at 150 °C, often produced catastrophic effects. It is well known that $CsHSO_4$ is soluble in liquid water, but it is thought that water vapor produces little effect. However, membranes of $CsHSO_4$ that were exposed to water vapor lost structural integrity, even in water to air concentrations as low as 20%. In fact, to prevent interaction between $CsHSO_4$ membranes and any ambient moisture that might have migrated from the lab atmosphere into the experimental tubing, all tubes were flushed with dry nitrogen at 150 °C for several hours before membranes were added to the permeation cell and experiments were run.

Since permeation to neutral species (such as methane) change after exposure to methanol, it was investigated whether methanol could also improve the survivability of a $CsHSO_4$ membrane in the presence of steam. A feed stream of 50/50 methanol/water was fed to the permeability cell, containing a $CsHSO_4$ membrane that had been treated with methanol, for periods of time, between which methane permeability runs were performed just as before.

The $CsHSO_4$ membrane resisted the methanol/water stream for two hours. The third hour of exposure, however, showed a marked increase in methane permeability. By the fourth hour, the permeation profile was closer to that of an untreated membrane. Additional exposure beyond four hours did not drastically degrade the membrane any further.

The resulting methane permeation profiles for steadily increasing exposure times for steam are shown in Figure 3.5 below.

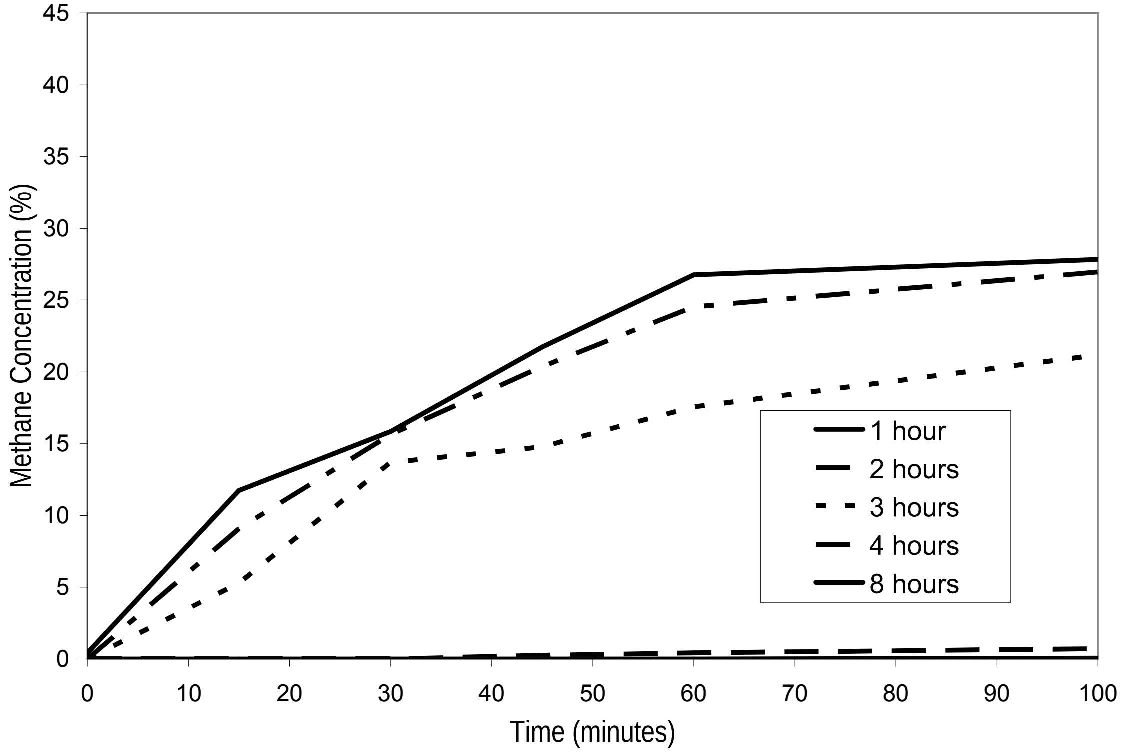

Figure 3.5 Effect of 50/50 Mix of Methanol/Steam on Permeability to Methane
Methane concentrations in the acceptor side of the permeability cell versus time for a methanol-treated membrane of $CsHSO_4$ after increasing exposures to 50/50 methanol/water.

4 Fuel Cell and Electrolysis Applications

The previous two chapters have described methods for the evaluation of the synthesis and optimization of $CsHSO_4$ as an electrolyte in membrane electrode assemblies. The following chapter will explore construction techniques of MEAs and will evaluate the performance of several fully constructed MEAs in a variety of applications. Specifically, the use of $CsHSO_4$ in an MEA for a H_2/air fuel cell and the electrolysis of methanol and steam will be explored.

4.1 Experimental Setup

A fuel cell test bed from the Fuel Cell Store (product FC25-01DM) with direct methanol capability was used for all fuel cell and electrolysis testing. Temperature was regulating using thermal pads included in the kit, as well as a Yamato DX300 Gravity Convection Oven, which also served to keep the inlet gas streams by heating long coils present in the oven. All experiments were conducted at 150 °C.

4.1.1 Fuel Cell

The performance of the fuel cell experiments was determined by measuring the electric potential and current across a variable resistor using a Yokogawa WT230 Digital Power Meter. Open cell voltage was measured by removing the resistor from the current. A schematic of the experimental setup is shown in Figure 4.1.

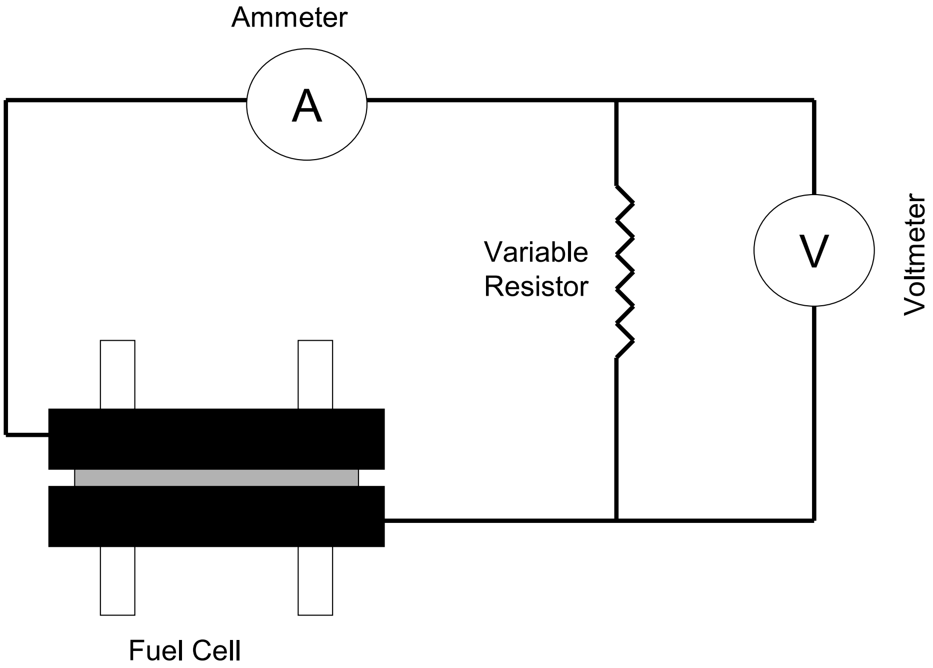

Figure 4.1 Circuit Diagram for Polarization Measurements of Fuel Cell
Experimental setup for measuring electric potential and current across load from a given fuel cell configuration.

4.1.2 Electrolysis

Direct current for electrolysis reactions was provided by an Agilent E3640A DC Power Supply, which also provided current flow through the electrolyte.

4.2 MEA Construction

MEAs for electrolysis and fuel cell experiments were constructed in the same way. Electrolyte membranes and electrode/catalyst assemblies were fabricated separately and then placed together in the fuel cell test bed. When the test bed was closed and tightened, this produced a single membrane electrode assembly.

4.2.1 Electrolyte

All electrolyte used in the following experiments was $CsHSO_4$ synthesized as described in Appendix A. Based on the ease of crystallization, and a desire to avoid any negative changes associated with the superprotonic phase change as shown in Chapter two with DSC, all electrolyte was crystallized out of solution by adding acetone. Two inch diameter, one millimeter thick $CsHSO_4$ membranes were uniaxially pressed with 100 tons of force, to create a densely-packed solid acid disc.

4.2.2 Electrodes

Carbon fiber paper was used as electrode material. Two inch diameter discs were cut from larger sheets of density 12 g/m^2 provided by Technical Fibre Products. These electrodes were then impregnated with catalyst material before being integrated into the completed MEA.

4.2.3 Catalysts

A mixture of platinum black, carbon black, naphthalene, and $CsHSO_4$ in a mass ratio of 10:1:1:6. This mixture was added to small amount of water to create a thick slurry. This slurry was spread onto the surface of the carbon fiber electrode. The electrode was then placed onto a crystal filter over a vacuum flask. The imposed vacuum pulled water through the fiber electrode, leaving the catalyst mixture impregnated throughout the mesh. The impregnated electrode was then dried in a convection oven at 70 ºC for several hours. This left carbon fibers coated with electrolyte, catalyst, carbon black, and naphthalene. The electrolyte improved electrical connection between the bulk electrolyte membrane and the catalyst, while the carbon black improved electrical connection between the catalyst and the electrode. When the MEA is heated to operating temperature (150 ºC) the naphthalene evaporates out of the catalyst layer, leaving a porous structure to increase available active sites.

A schematic of the catalyst impregnation process into a carbon fiber electrode is shown in Figure 4.2 below.

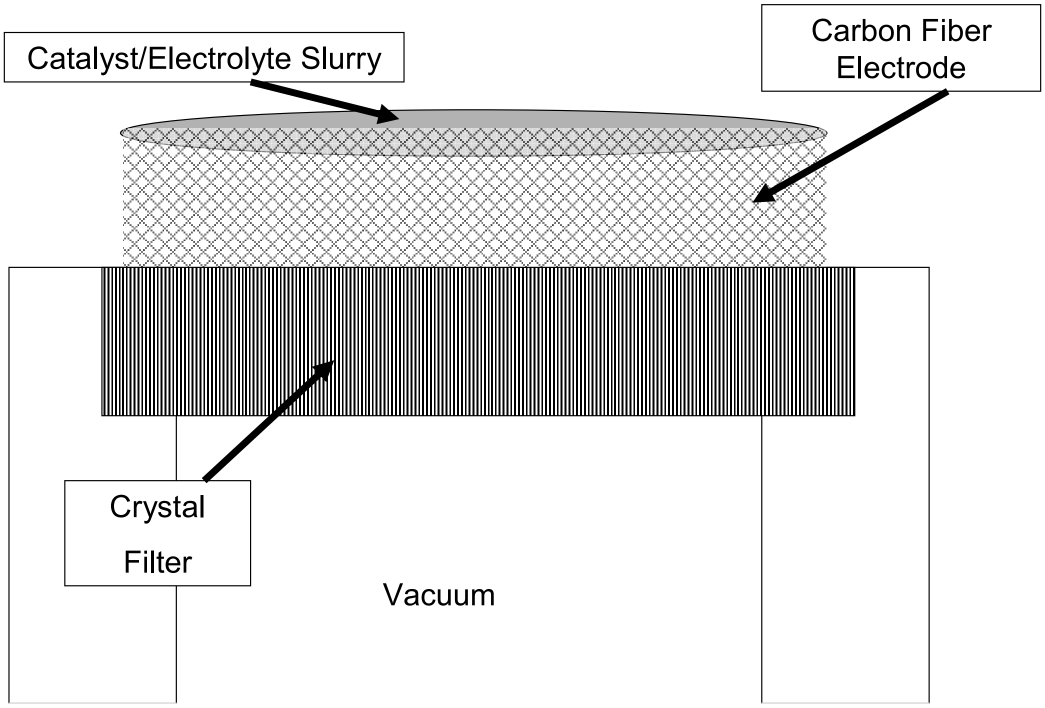

Figure 4.2 Catalyst/Electrode Construction
A catalyst slurry of platinum black, carbon black, electrolyte, and naphthalene is pulled by vacuum into a carbon fiber electrode, creating a porous electrode/catalyst assembly with superior electrolyte to catalyst and catalyst to electrode connection.

4.3 Fuel Cell Performance

The following is experimental polarization curves of H_2/O_2 fuel cells with $CsHSO_4$-based membrane electrode assemblies with a variety of preparation methods.

Figure 4.3 below shows a polarization curve of a freshly-made MEA.

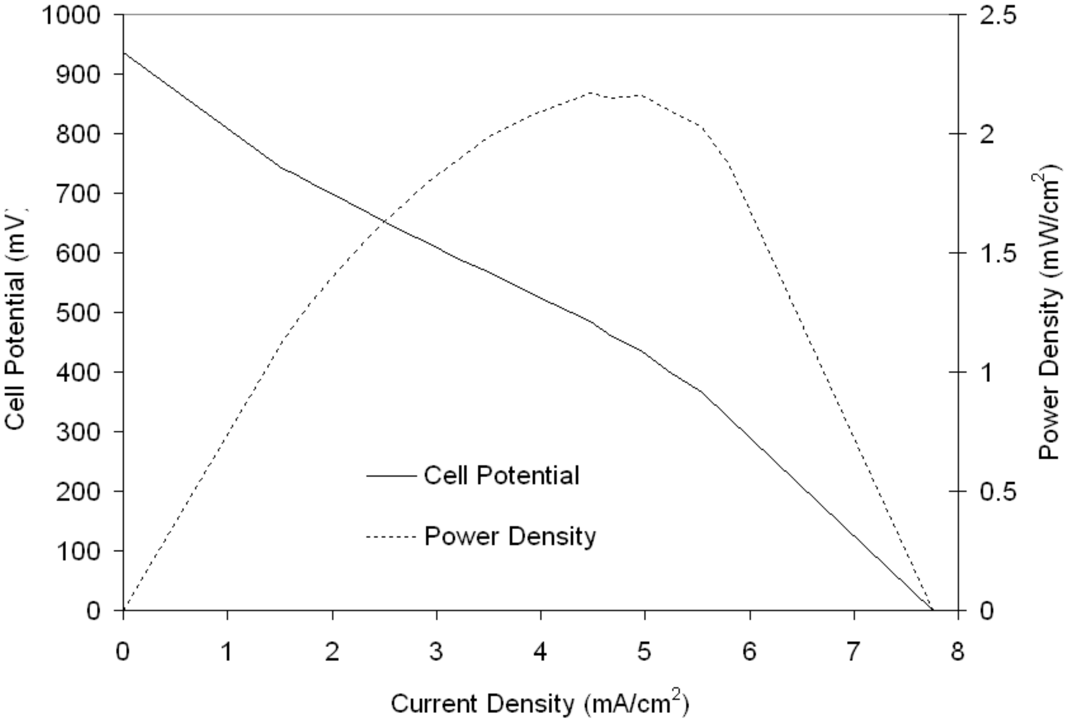

Figure 4.3 Polarization Curve of $CsHSO_4$ Fuel Cell with H_2 and Air
Electric potential and power density with increasing current density of a freshly made $CsHSO_4$ MEA.

This MEA shows an open cell voltage that approaches ideal (1.17 V), but current density, and by extension, power density is low.

A H_2/O_2 polarization curve was generated with an MEA that had been used in the electrolysis of methanol (see next section). It is shown in Figure 4.4 below.

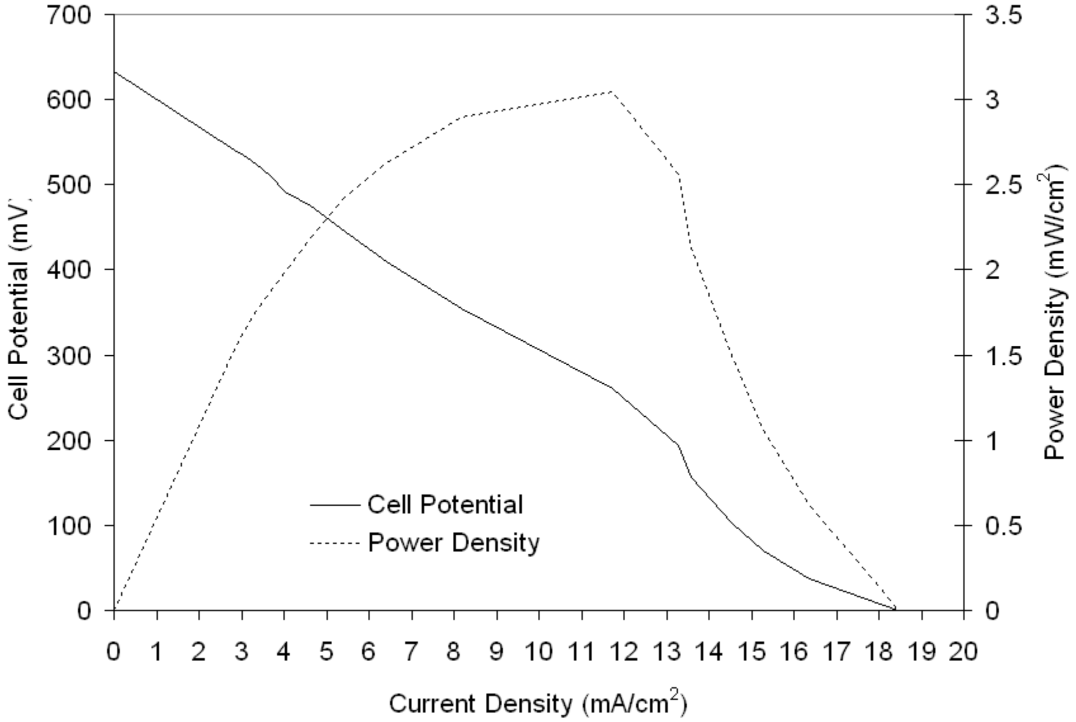

Figure 4.4 Polarization Curve of $CsHSO_4$ Fuel Cell with H_2 and Air after Methanol Electrolysis

Electric potential and power density with increasing current density of a $CsHSO_4$ MEA after use in methanol electrolysis.

This is compared to a similar polarization curve of a $CsHSO_4$ MEA that had been simply treated with a long exposure to methanol at high temperature in a manner similar to the permeability tests (Chapter 3). This curve is shown in Figure 4.5 below.

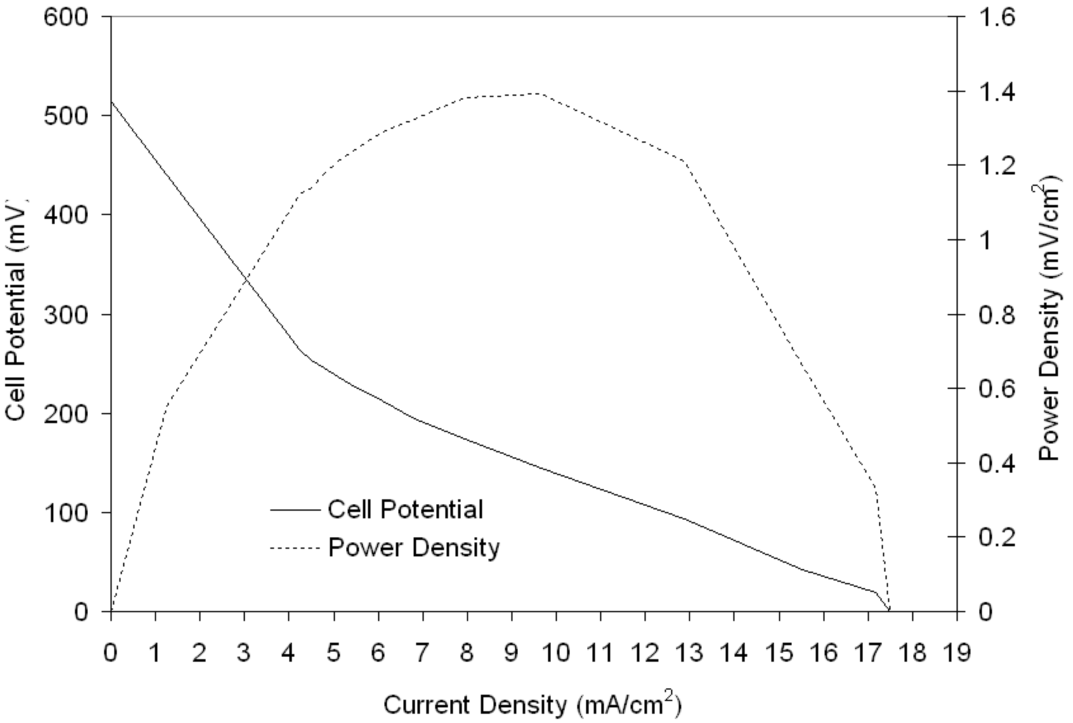

Figure 4.5 Polarization Curve of $CsHSO_4$ Fuel Cell with H_2 and Air after Methanol Sintering (Long-term)
Electric potential and power density with increasing current density of a $CsHSO_4$ MEA after methanol treatment.

These two polarization curves show a marked reduction in open-cell voltage, being a little over half that observed for a fresh MEA. However, current density is increased.

The MEA in the previous experiment was subjected to a longer stream of hydrogen while under load for several hours. With time, open cell voltage increased, although not back to the pre-methanol treatment levels. Current density remained similar to that of a treated MEA, resulting in a higher maximum power density. This polarization curve is shown in Figure 4.6.

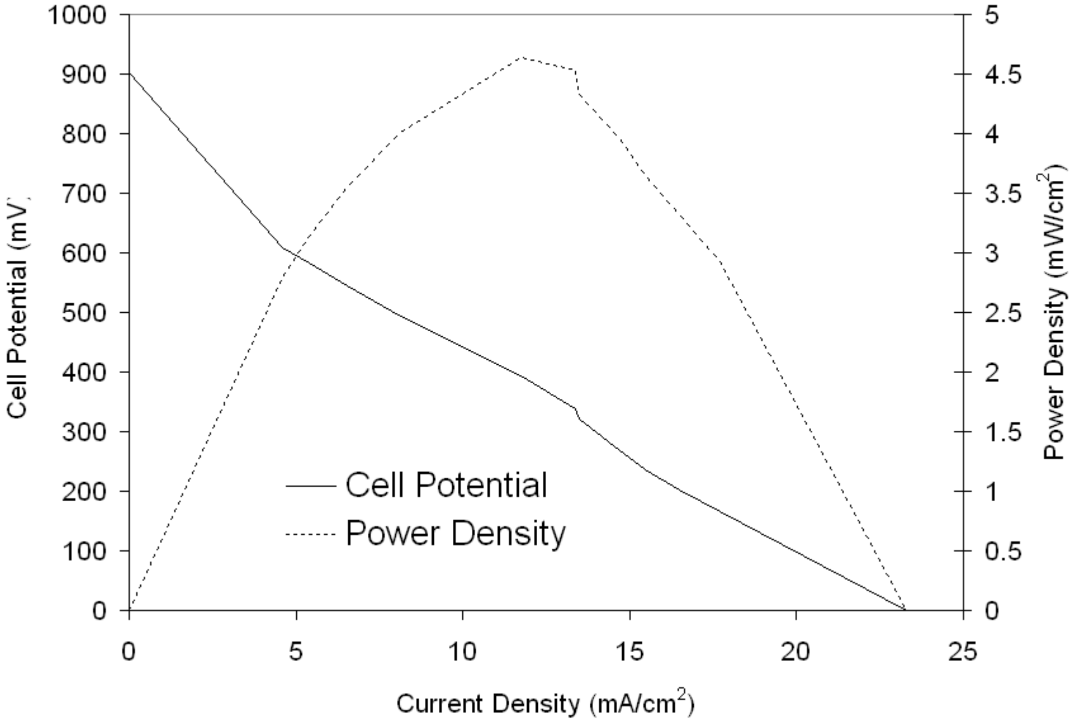

Figure 4.6 Polarization Curve of $CsHSO_4$ Fuel Cell with H_2 and Air after Methanol Sintering and Regeneration
Electric potential and power density with increasing current density of a $CsHSO_4$ MEA after methanol treatment

Data from these polarization curves is summarized in Table 4-1 below.

Table 4-1 Fuel Cell Data

Cell Run	Open Cell Voltage (mV)	Efficiency of Open Cell (E_V)	Maximum Current Density (mA/cm^2)	Maximum Power Density			
				Cell Potential (mV)	Efficiency (E_V)	Current Density (mA/cm^2)	Power Density (mW/cm^2)
Fresh $CsHSO_4$ MEA	936	80.0%	7.76	485	41.5%	4.48	2.17
MEA post methanol electrolysis	633	54.1%	18.4	260	22.2%	11.7	3.05
MEA after methanol treatment	514	43.9%	17.5	144	12.3%	9.67	1.39
Treated MEA after extended H_2 exposure	902	77.1%	23.3	395	33.8%	11.8	4.64

4.4 Electrolysis Performance

MEAs made with the construction methods described earlier were also used in electrolysis application using much of the same experimental setup. Methanol and steam electrolysis were investigated.

4.4.1 Electrolysis of Methanol

Methanol electrolysis was performed using a 50/50 mix of water vapor and methanol. The following figures show how measured current density increased after minimum voltage was applied.

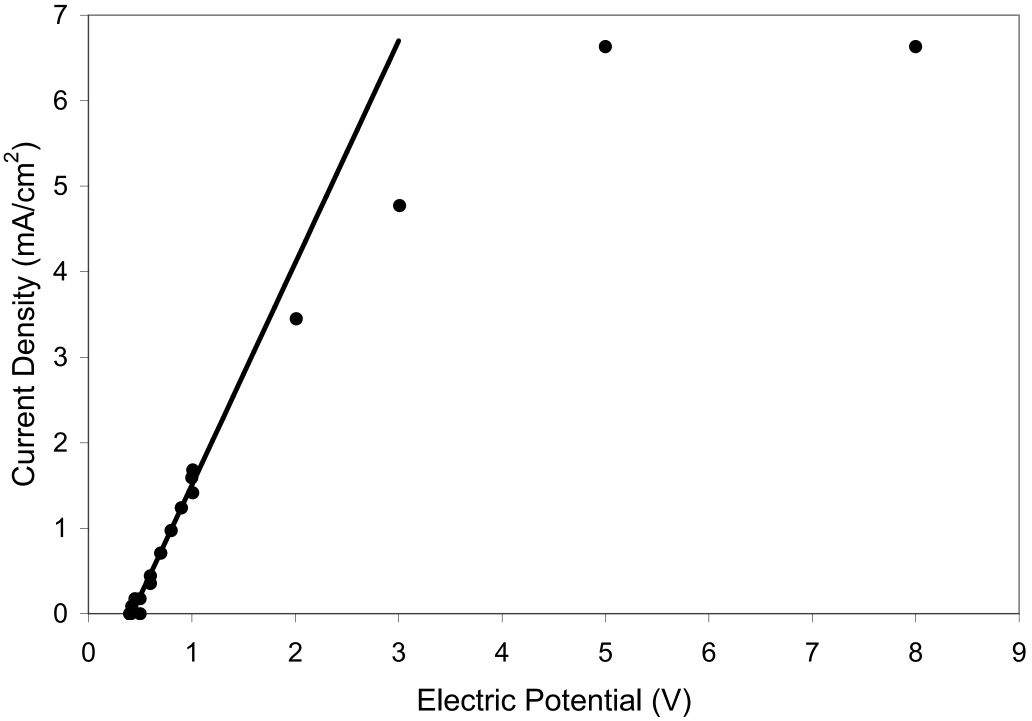

Figure 4.7 Electrolysis of Methanol
Current density and power density versus increasing voltage for the electrolysis of methanol.

Figure 4.8 shows the behavior of current density versus increasing voltage just above the minimum voltage for methanol electrolysis.

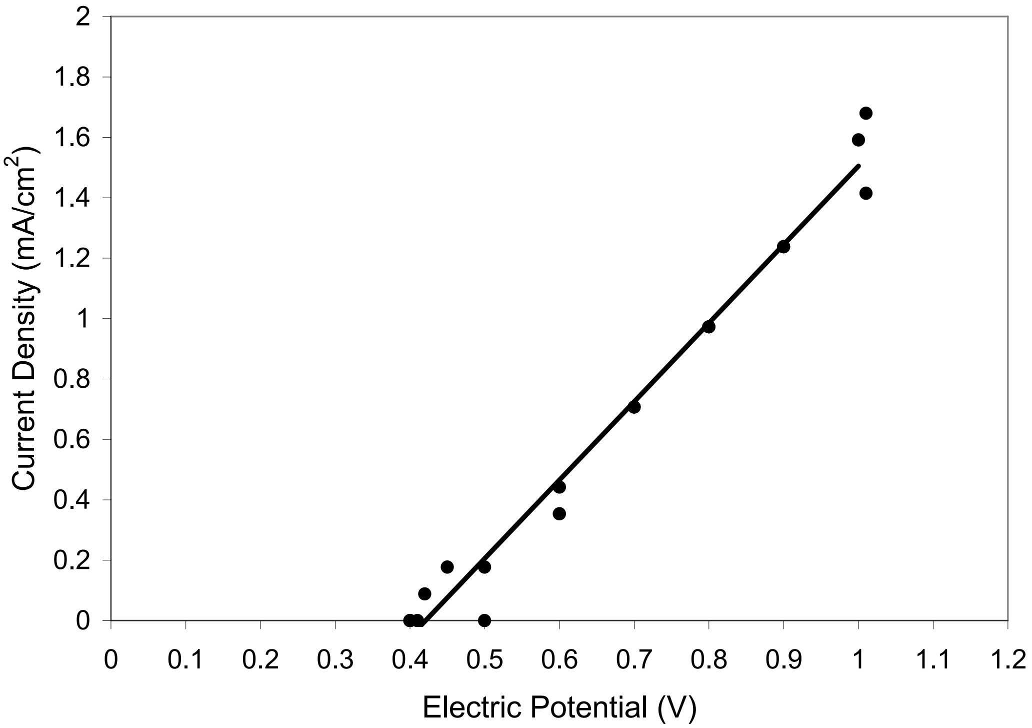

Figure 4.8 Electrolysis of Methanol at Low Voltage
Electrolysis of methanol at lower voltages showing minimum voltage required.

4.4.2 Electrolysis of Steam

The following figures show increasing current density with increasing applied voltage for the electrolysis of steam. Feed flows were 10/90 methanol/water vapor in an effort to prevent structural degradation of $CsHSO_4$ upon contact with water vapor.

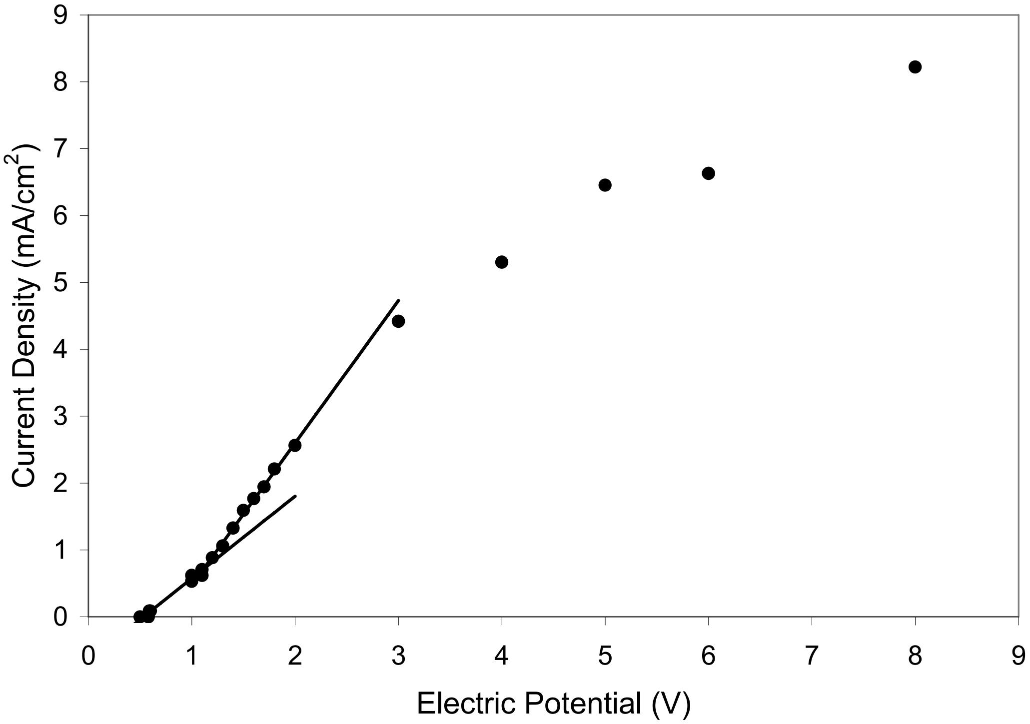

Figure 4.9 Electrolysis of Steam
Current density and power density versus increasing voltage for the electrolysis of steam.

Figure 4.10 shows the behavior of current density versus increasing voltage just above the minimum voltage for electrolysis of steam.

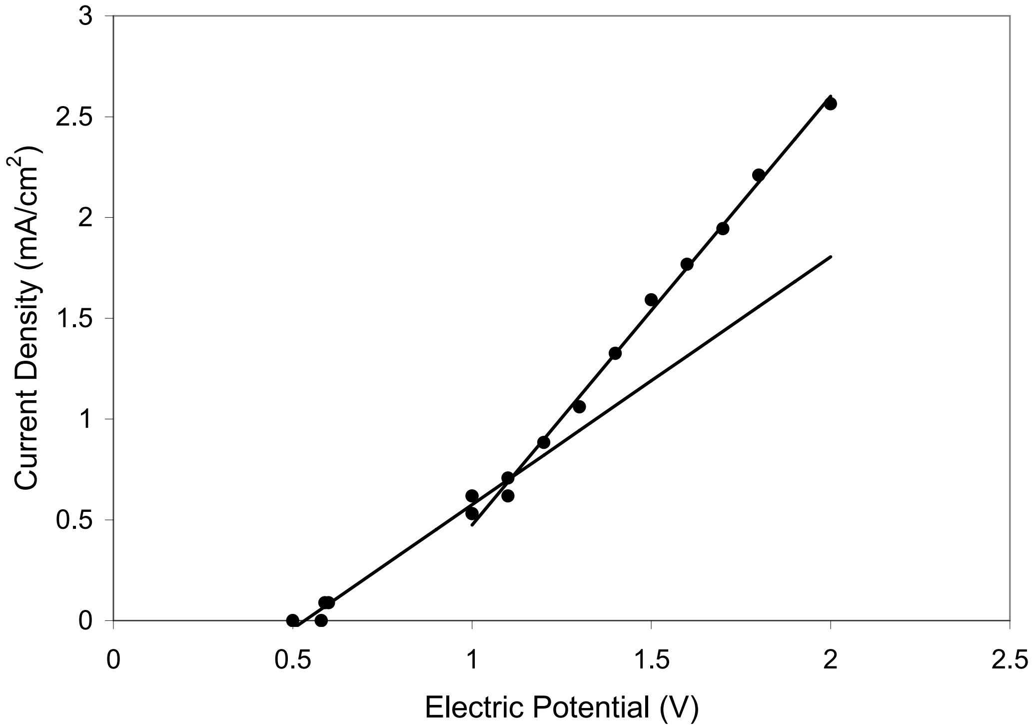

Figure 4.10 Electrolysis of Steam Low Voltage
Electrolysis of methanol at lower voltages showing minimum voltage required.

Notable on the plot of current versus electric potential for the electrolysis of steam is the low minimum voltage for current flow, at approximately 0.6 volt. The linear relation of current to voltage takes a quick upturn, and begins rising at a steeper slope, after 1.3 volts.

5 Summary and Conclusions

The following chapter will present the conclusions derived from the data presented in Chapters 2, 3, and 4. These conclusions are separated by chapter subject, so will proceed from materials characterization, to permeability studies, to conclusions about the fuel cell and electrolysis applications. Finally, some suggestions for future directions for further research based on the findings of this work will be presented.

5.1 Materials Characterization

The primary conclusions of the material characterization methods of $CsHSO_4$ are presented below. $CsHSO_4$ was investigated with impedance spectroscopy, differential scanning calorimetry (DSC), thermal gravimetric analysis (TGA), powder X-ray diffraction (PXRD), and X-ray photoelectron spectroscopy (XPS) in order to determine the relative benefits and problems associated with the different synthesis and pressing methods investigated. A secondary goal with materials characterization was the determination of feasibility and applicability of the different characterization methods to $CsHSO_4$ as part of an effort to design a consistent, efficient characterization procedure for future samples.

Crystallization by introduction of organic produces smaller crystallite sizes than those produced by slow evaporation, while crystals produced using acetone were easier to dry producing acceptable material. Crystals produced with methanol or with water tended to clump together, and had to be aggressively ground and dried.

Slight variations were observed between different crystallization and pressing conditions with impedance spectroscopy. Membranes that had been crystallized by acetone showed improved proton conductivity against those that were crystallized by temperature control, while membranes that had been pressed under heated conditions were still better. Since proton conductivity can be determined from thermodynamic and structural constants, one would expect all samples of $CsHSO_4$ to display identical proton conductivity at a given temperature. The primary difference is, however, that samples investigated in this work were all pressed powders and non single crystals. Interface gaps between crystallites, variation in the orientation of crystallites, and gaps between larger flakes of clumped crystallites would all result in different measured properties from impedance spectroscopy.

It is also notable that despite the differences that these different constants would impose, that the ultimate proton conductivities at 150 °C for all samples were similar values. This result allows whichever production method that is the easiest, most efficient, or most economical to be chosen without concern of undue effect on proton conductivity.

Loss of mass in the superprotonic phase was observed with TGA consistent with the degradation of $CsHSO_4$ to $Cs_2S_2O_7$ and water. This loss was also associated with an endothermic peak on DSC. When the sample was tested in DSC with a closed cup to prevent evolution of water, or when the sample was retried in an open cup immediately after a previous experiment, this loss of mass was not observed. This leads to the conclusion that $CsHSO_4$ in the superprotonic phase will evolve water, degrading to $Cs_2S_2O_7$, particularly in the presence of dry fuel or oxidant streams. Special consideration should be paid to the effect of the evolution of water in operating conditions, as $Cs_2S_2O_7$ lacks the proton conductivity of $CsHSO_4$.

The jagged peaks observed on DSC with samples that had been crystallized by temperature variation suggest a structural effect on the evolution of water in the superprotonic phase. Given the greater tendency for $CsHSO_4$ that has been crystallized by temperature variation to clump into larger pieces, this jagged profile may be due to pockets of moisture forming within the powder clumps as with other samples. With the greater clumping, however, these moisture pockets build up pressure within the clump, and are then released in bunches, resulting in many small endothermic peaks observed by DSC. So, in addition to worrying about the effect of the evolution of water has on the proton conductivity of $CsHSO_4$, an additional problem with samples that have been crystallized by temperature control is the effect on structural integrity of the membrane from this physical bursting as water is released.

Phases were identified using PXRD. Solid matching of experimental patterns with reference patterns for $CsHSO_4$-III and $CsHSO_4$-II confirmed the reproducibility of structural features from synthesis methods. Also present were samples that showed peaks associated with both $CsHSO_4$-III and $CsHSO_4$-II, meaning that samples of mixed phases were also produced.

$CsHSO_4$-II was found in those samples that had been aggressively dried at temperatures in excess of 70 °C, while those that were not as aggressively dried (typically those samples that were crystallized using acetone) showed just the $CsHSO_4$-III phase. The time frame between when aggressively dried samples were removed from the drying oven and when they were investigated with PXRD, occasionally a period of days, suggests that the phase change from $CsHSO_4$-III to $CsHSO_4$-II is essentially irreversible.

Although XPS survey scans produced characteristic peaks that would be expected for cesium and oxygen, the sulfur peaks were obscured by much larger cesium peaks that have similar binding energy. This made using XPS to determine atomic ratios and chemical shifts, and therefore the presence of excess acid, crystallizing agents, or surface reactants with different crystallization methods problematic.

A standardized production procedure was established for $CsHSO_4$ membranes for use in all future work. Synthesis of $CsHSO_4$ from Cs_2SO_4 was chosen as this was an easier and safer reaction than that of synthesis from Cs_2CO_3. From the results of materials characterization tests it was decided that all standard synthesis would use acetone-crystallized $CsHSO_4$, instead of those crystallized by methanol or temperature variation. The primary factors for this choice were the ease of use of acetone crystallization, and concerns about the effects of clumping flakes, particularly after the superprotonic transition as observed by DSC and TGA. Pressing conditions can be chosen based on the ease of manufacture, as significant changes in membrane conductivity were seen to be independent of the pressing method.

For the evaluation of completed $CsHSO_4$ samples, use of PXRD and DSC/TGA produced the most useful results. Conductivity tests confirmed the presence of $CsHSO_4$ and its superprotonic character with the higher temperature phase, but did not show much variation between different sample histories or easily repeatable results. XPS was hindered by the overlapping of photoelectron peaks from cesium over those from sulfer, limiting its use as a diagnostic tool. PXRD and DSC/TGA, however, allowed for the evaluation of phase presence, crystallite size, and the dynamics of dehydration at higher temperatures. These methods show a good promise for the robust evaluation of the quality of future $CsHSO_4$ samples.

5.2 Permeability Studies

The results and conclusions of methanol and methane permeability studies are presented below. Permeability to fuel and oxidant gases goes directly to the performance of a given electrolyte within an MEA. Excessive permeability in an MEA can lower the current density and the output electric potential for a fuel cell.

$CsHSO_4$ membranes created using the standard procedure developed from Chapter 2 proved to be highly permeable to gases. Flux of gases across the surface of the membrane was sufficient to cause a large change in concentration on the other side of the membrane in the space of minutes. Membranes with this high degree of permeability would not be suitable as MEAs in fuel cells.

Those membranes that were exposed to methanol at high temperatures, later showed a remarkable reduction in their permeability. Flux of fuel gas across their surface was reduced by nearly three orders of magnitude, and the membranes could be run in the cell for hours with only a slight change in the concentration of gases on the acceptor side of the cell. This change seems irreversible, as membranes so treated kept these permeability characteristics long after the initial runs were completed, and later runs, up to days later, showed similar results.

Membranes treated with methanol also showed increased resistance to water vapor. Untreated membranes, when exposed to water vapor, would lose their structural integrity and collapse into a loose deposit on the bottom of the cell within minutes of exposure. Treated membranes could withstand a 50/50 water vapor/methanol mix for up to three hours before showing any effect. Even this situation, membranes showed an increased permeability to neutral gases (methane), and not a total collapse like untreated membranes.

These results lead to the conclusion that a fuel cell of electrolysis process that would use $CsHSO_4$ as an electrolyte should include treatment with methanol, or a similar treatment process to prevent a highly permeable MEA. The result of increased resistance to water vapor is also promising, as it allows for the use of $CsHSO_4$ in a direct methanol fuel cell, which requires water vapor in the fuel stream to allow complete reaction on the anode.

5.3 Fuel Cell and Electrolyte Test Bed

H_2/O_2 fuel cells were successfully run with $CsHSO_4$ MEAs. These produced fuel cells with open cell voltages that were close to the expected values (1.17 V), but with much lower current densities than that of commercial fuel cells using Nafion© or phosphoric acid. These lower current densities may be due to gas permeability of the untreated $CsHSO_4$. Flow of fuel gas to the cell reaches a rate at which the fluid flow dynamics limit the amount of gas that can reach or escape the surface of the membrane, but a significant portion passes through the electrolyte without reaction, resulting in a lower observed current.

Membranes that had been exposed to methanol at high temperatures, either through the treatment method developed in Chapter 3, or as a result of the methanol electrolysis experiment, showed an increase in current density, but a decrease in open cell voltage. The increase in current could be a result of the decrease in permeability to fuel gases leading to a greater proportion of the gases reacting at the surface versus passing through the membrane without reacted.

The decrease in observed open cell voltage is more problematic, as it implies that the methanol treatment may cause a change in the proton transport mechanism of membranes so treated. A possible explanation is that methanol absorbed during the treatment phase is reacting to produce formaldehyde within the electrolyte. Since methanol is permeable through a fresh membrane, it may be present in the electrolyte to some depth. Methanol can react in an anode reaction to produce hydrogen and formaldehyde, followed by the hydrogen being transported through the electrolyte as in the simple dissociation of molecular hydrogen:

$$CH_3OH \rightarrow HCHO + 2H^+ + 2e^-$$

If this reaction is not in equilibrium, which given the finite amount of absorbed methanol that would remain following the treatment, a reduction in observed voltage can occur, as protons evolved by this reaction produce a potential back through the electrolyte, similar to an activation polarization. It is difficult to estimate the exact amount that this may actually reduce the observed potential, however, because of lack of data of the amount of methanol so entrained. The ideal potential of a half-cell with this reaction is only 0.189 volts, but if the amount of methanol is greater than the available reaction sites for hydrogen as a fuel gas, there may be a stoichiometrically greater amount of methanol reacting than hydrogen, causing a larger voltage.

Other possibilities include the creation of an oxide or other chemical reaction between methanol and $CsHSO_4$, or poisoning of the platinum catalyst. The creation of an oxide layer should not change the open cell voltage of the cell, but may produce a profound lowering of voltage with current due to Ohmic polarization or activation polarization due to changing surface chemistry. Catalyst poisoning essentially competes with hydrogen for reaction sites, which also is seen primarily at higher currents, but since the catalyst is part of the electrode assembly, poisoning of the catalyst might also reduce observed voltage by creating an electric potential gradient within the electrode.

When runs were continued with hydrogen and oxygen with treated membranes for longer periods, observed potentials increased. If the lowered potential was due to the formation of formaldehyde, than the gradually lowering methanol concentration could explain this rise. Cell potentials never returned to those of fresh membranes, suggesting that additional losses due to chemical reaction of methanol and $CsHSO_4$ or catalyst poisoning might be present.

Electrolysis reactions for methanol and steam were also successful. Methanol electrolysis began at 0.4 volts, but consistent current was not seen until the potential was raised to over 0.6 volts, after which current increased linearly with potential. Maximum current density was achieved at approximately 6 volts, caused by the limits of gas transport either to or from the surface of the membrane.

Electrolysis of steam first showed current as low as 0.6 volts, significantly lower than the expected 1.2 or greater. Notably, the linear relation of current to voltage increases significantly at voltage higher than 1.3 volts. The lower current from 0.6 to 1.3 volts is most likely the result of methanol in the feed (10% methanol was used in the feed to prevent $CsHSO_4$ from losing structural integrity). After the potential was raised to allow the dissociation of water, higher currents were observed. Like with methanol electrolysis, a maximum current was eventually achieved due to limits of gas transport to and from the surface of the membrane.

The successful use of $CsHSO_4$ in fuel cell and electrolysis applications in this work represents a confirmation of the feasibility of $CsHSO_4$ as a proton conducting electrolyte in real applications. As of this work, the successful use of $CsHSO_4$ has been reported at the California Institute of Technology[2, 4]. Data presented in this work affirms this finding.

5.4 Future Directions

The ability to construct workable applications for $CsHSO_4$ in a laboratory setting shows the potential of $CsHSO_4$ as a proton conducting electrolyte has value for future research. Problems with fuel gas permeability, chemical stability in the superprotonic phase, and current density have to be overcome, but there is ample evidence that a $CsHSO_4$ based MEA could provide significant advantage over current commercial MEAs in specialty applications.

Although its use in competitive fuel cells is in question due to low current densities and losses due to polarization, $CsHSO_4$ may still prove useful in specialty applications where its operational temperature range (144 to 180 °C) allows for a special advantage that cannot be realized by existing electrolytes like Nafion© or phosphoric acid. One example would be the electrolysis of hydrogen sulfide, a toxic byproduct of certain electricity generation processes that must be aggressively treated with stack scrubbers to conform to EPA regulations. H_2S can be electrolyzed in a reaction similar to the electrolysis of steam:

$$H_2S \rightarrow H_2 + S$$

Sulfur is a liquid at temperatures in excess of 115 °C, allowing product sulfur to pour out of an electrolysis cell, where it might be collected as a commercial product. With sulfur and hydrogen as reaction products, this process might be considered as both a pollution control step and a commercial chemical production step. As an added advantage, reaction and separation is combined into a single process negating the need for an additional gas separation step. Other specialized reactions requiring ion mobility from heterogeneous reaction sites within the operational temperature range may be possible.

To determine any future feasibility of $CsHSO_4$ in any type of electrolysis process, the problems identified within this work would need to be addressed. The possibility of using a gaseous organic to improve permeability characteristics was explored. Unfortunately, this procedure produced unforeseen effects once performed on an MEA in a real application. It is currently unclear whether the loss of permeability and the loss of performance (open cell voltage) are related, or are due to separate effects. It is also unclear whether the change to $CsHSO_4$ as a result of exposure to methanol is physical, such as crystal growth, dehydration, or the absorption of methanol, or if the change is chemical, such as the production of cesium methyl sulfate:

$$CH_3OH + CsHSO_4 \rightarrow Cs(CH_3)SO_4 + H_2O$$

This reaction is similar to that already reported in literature[40] as possible between methanol and sulfuric acid, producing methyl hydrogen sulfate (this reaction may also be occurring with unreacted sulfuric acid still present in the electrolyte):

$$CH_3OH + H_2SO_4 \rightarrow (CH_3)HSO_4 + H_2O$$

Another possibility is poisoning of the platinum catalyst when exposed to methanol in the fuel cell configuration, which would not be a consideration with earlier permeability tests which did not include electrode or catalyst layers.

Whatever the exact effect that methanol has on $CsHSO_4$ membranes, there is no denying that the procedure improves impermeability. It is unclear if this effect is due to a chemical change in the electrolyte upon exposure to methanol, or a physical change. It is known that $CsHSO_4$ crystallizes out of aqueous solution when an organic such as methanol is introduced. A similar physical reaction of crystal growth promotion may be occurring when the polycrystalline sample is exposed to gaseous methanol. The ability of $CsHSO_4$ to absorb moisture from the laboratory environment was a constant concern during experiments. If water is absorbed into the membrane during normal handling procedures (deliquescence), this may partially dissolve $CsHSO_4$ within the membrane. When exposed to methanol, this partially dissolved $CsHSO_4$ would then precipitate back out of solution, its crystal growth sealing gaps between grains within the polycrystalline sample. Although the interaction with methanol seems to produce unintended losses of performance, the possibility exists that other gaseous organic solvents may also have a beneficial effect on $CsHSO_4$ or other solid acid electrolytes without these losses. The interaction of various organic vapors on different solid acid electrolytes and catalysts for permeability and performance characteristics is an area of future investigation.

References

[1] T. Norby, The Promise of Protonics, *Nature*, 410, 877-878, 2001.

[2] S. M. Haile, D. A. Boysen, C. R. I. Chisholm, and R. B. Merle, Solid Acids as Fuel Cell Electrolytes, *Nature*, 410(6831), 910–913, 2001.

[3] X. Ke and I. Tanaka, Proton Transfer Mechanism in Solid $CsHSO_4$ by First-Principles Study, *Solid State Ionics*, 172(1-4), 145-148, 2004.

[4] D. A. Boysen, *Superprotonic Solid Acids: Structure, Properties, and Applications,* California Institute of Technology, 2004.

[5] S. Hayashi and M. Mizuno, Proton Diffusion in the Superprotonic Phase of $CsHSO_4$ Studied by ^{1}H NMR Relaxation, *Solid State Ionics*, 171(3-4), 289-293, 2004.

[6] M. Mizuno and S. Hayashi, Proton Dynamics in Phase II of $CsHSO_4$ Studied by ^{1}H NMR, *Solid State Ionics*, 167(3-4), 317-323, 2004.

[7] A. V. Belushkin, R. L. McGreevy, P. Zetterstrom and L. A. Shivalov, Mechanism of Superprotonic Conductivity in $CsHSO_4$, *Physica B: Condensed Matter*, 241-243, 323-325, 1997.

[8] W. Münch, K. D. Kreuer, U. Traub and J. Maier, Proton Transfer in the Three-Dimensional Hydrogen Bond Network of the High Temperature Phase of $CsHSO_4$: A Molecular Dynamics Study, *Journal of Molecular Structure*, 381(1-3), 1-8, 1996.

[9] T. Norby, M. Friesel and B. E. Mallander, Proton and Deuteron Conductivity in $CsHSO_4$ and $CsDSO_4$ by In Situ Isotopic Exchange, *Solid State Ionics*, 77, 105-110, 1995.

[10] L. Kirpichnikova, M. Polomska, J. Wolak and B. Hilczer, Polarized Light Study of the $CsHSO_4$ and $CsDSO_4$ Superprotonic Crystals, *Solid State Ionics*, 97(1-4), 135-139, 1997.

[11] A. V. Belushkin, M. A. Adams, S. Hull and L. A. Shuvalov, P-T Phase Diagram of $CsHSO_4$. Neutron Scattering Study of Structure and Dynamics, *Solid State Ionics*, 77, 91-96, 1995.

[12] J. Baran and M. K. Marchewka, Vibrational Investigation of Phase Transitions in $CsHSO_4$ Crystal, *Journal of Molecular Structure*, 614(1-3), 133-149, 2002.

[13] A. R. Lim, J. H. Chang, H. J. Kim and H. M. Park, Phase Transition and Ferroelastic Property Studied by Using the 133Cs Nuclear Magnetic Resonance in a $CsHSO_4$ Single Crystal, *Solid State Communications*, 129(2), 123-127, 2004.

[14] V. Varma, N. Rangavittal and N. R. Rao, A Study of Superionic $CsHSO_4$ and $Cs_{1-x}Li_xHSO_4$ by Vibrational Spectroscopy and X-ray Diffraction, *Journal of Solid State Chemistry*, 106, 164-173, 1993.

[15] N. Rangavittal, T. N. Guru Row, and C. N. R. Rao, Thermally Induced Phase Transitions of $CsHSO_4$: A Reexamination, *Journal of Solid State Chemistry*, 117, 414-415, 1995.

[16] B. Baranowski and J. Lipkowski, On the Phase Transitions of Cesium Hydrogen Sulfate ($CsHSO_4$), *Journal of Solid State Chemistry*, 117, 412-413, 1995.

[17] C. R. I. Chisholm, *Superprotonic Phase Transitions in Solid Acids,* California Institute of Technology, 2002.

[18] C. R. I. Chisholm and S. M. Haile, X-ray Structure Refinement of $CsHSO_4$ in Phase II, *Materials Research Bulletin*, 35(7), 999-1005, 2000.

[19] A. V. Belushkin, M.A. Adams, S. Hull, A.I. Kolesnikov, L.A. Shuvalov, Structure and Dynamics of Different Phases of the Superprotonic Conductor $CsHSO_4$, *Physica B*, 213&214, 1034-1036, 1995.

[20] B. Yang, A. M. Kannan and A. Manthiram, Stability of the Dry Proton Conductor $CsHSO_4$ in Hydrogen Atmosphere, *Materials Research Bulletin*, 38(4), 691-698, 2003.

[21] I. N. Levine, *Physical Chemistry,* McGraw-Hill Book Company, New York, 1988.

[22] P. Schuster, G. Zundel, C. Sandorfy, *The Hydrogen Bond*, North-Holland Publishing Company, Amsterdam, 1976.

[23] R. E. Hummel, *Electronic Properties of Materials*, Springer-Verlag, Berlin Heidelberg, 1993.

[24] U.S. Department of Energy, *Fuel Cell Handbook*, National Energy Technology Laboratory, Strategic Center for Natural Gas, Morgantown WV, Pittsburgh, PA, Tulsa, OK, 2002.

[25] A. J. Appleby and F. R. Foulkes, *Fuel Cell Handbook*, Van Nostrand Reinhold, New York, 1989.

[26] J. Larminie and A. Dicks, *Fuel Cell Systems Explained, 2nd Ed.*, Wiley, West Sussex (2003).

[27] C. Berger, *Handbook of Fuel Cell Technology*, Prentice-Hall, Englewood Cliffs, NJ, 1968.

[28] J. R. MacDonald, *Impedance Spectroscopy*, Wiley, New York (1987).

[29] A. Guinier, *X-ray Diffraction in Crystals, Imperfect Crystals, and Amorphous Bodies*, Dover, New York, 1994.

[30] B. D. Cullity and S. R. Stock, *Elements of X-ray Diffraction*, Prentice-Hall, Upper Saddle River, NJ, 2001.

[31] J. Lipkowski, B. Baranowski, and A. Lunden, *Pol. J. Chem.*, 67, 1867, 1993.

[32] V.I. Nefedov, *X-ray Photoelectron Spectroscopy of Solid Surfaces*, Utrecht, Netherlands, 1988.

[33] J. G. Ferreira and M. T. Ramos, *X-ray Spectroscopy in Atomic and Solid State Physics*, Plenum Press, New York, 1988.

[34] J. F. Moulder, W. F. Stickle, P. E. Sobol, and K. D. Bomben, *Handbook of X-ray Photoelectron Spectroscopy*, Physical Electronics, Inc., USA (1995).

[35] V. Tricoli, Proton and Methanol Transport in Poly(perfluorosulfonate) Membranes Containing Cs^+ and H^+ Cations, *J. Electrochem. Soc.*, 145, 3798 (1998).

[36] J. Crank and G.S. Park, *Diffusion in Polymers*, Academic Press, London (1968).

[37] M. Mulder, *Basic Principles of Membrane Technology*, Kluwer Academic Publishers, Dordrecht, Netherlands (1991).

[38] R. L. Grob, *Modern Practice of Gas Chromatography*, Wiley-Interscience, New York, 1995.

[39] D. Ambrose, *Gas Chromatography*, Butterworths, London, 1971.

[40] L. L. Van Loon and H. C. Allen, Methanol Reaction with Sulfuric Acid: A Vibrational Spectroscopic Study, *J. Phys. Chem. B*, 108(45), 17666-17674, 2004.